nature nanotechnology

SUPPLEMENTARY INFORMATION

https://doi.org/10.1038/s41565-019-0604-x

In the format provided by the authors and unedited.

Lithium whisker growth and stress generation in an in situ atomic force microscope–environmental transmission electron microscope set-up

Liqiang Zhang[1,2,6], Tingting Yang[1,6], Congcong Du[1], Qiunan Liu[1], Yushu Tang[2], Jun Zhao[1], Baolin Wang[3], Tianwu Chen[4], Yong Sun[1], Peng Jia[1], Hui Li[1], Lin Geng[1], Jingzhao Chen[1], Hongjun Ye[1], Zaifa Wang[1], Yanshuai Li[1], Haiming Sun[1], Xiaomei Li[1], Qiushi Dai[1], Yongfu Tang[1]*, Qiuming Peng[1], Tongde Shen[1], Sulin Zhang[4]*, Ting Zhu[3]* and Jianyu Huang[1,5]*

[1]Clean Nano Energy Center, State Key Laboratory of Metastable Materials Science and Technology, Yanshan University, Qinhuangdao, China. [2]State Key Laboratory of Heavy Oil Processing, China University of Petroleum Beijing, Beijing, China. [3]Woodruff School of Mechanical Engineering, Georgia Institute of Technology, Atlanta, GA, USA. [4]Department of Engineering Science and Mechanics, Pennsylvania State University, University Park, PA, USA. [5]Key Laboratory of Low Dimensional Materials and Application Technology of Ministry of Education, School of Materials Science and Engineering, Xiangtan University, Xiangtan, China. [6]These authors contributed equally: Liqiang Zhang, Tingting Yang.
*e-mail: tangyongfu@ysu.edu.cn; suz10@engr.psu.edu; ting.zhu@me.gatech.edu; jyhuang8@hotmail.com

Supplementary Information

Lithium whiskers growth and stress generation in an in situ atomic force microscope-environmental transmission electron microscope setup

Liqiang Zhang, Tingting Yang, Congcong Du, Qiunan Liu, Yushu Tang, Jun Zhao, Baolin Wang, Tianwu Chen, Yong Sun, Peng Jia, Hui Li, Lin Geng, Jingzhao Chen, Hongjun Ye[1], Zaifa Wang, Yanshuai Li, Haiming Sun, Xiaomei Li, Qiushi Dai, Yongfu Tang[*], Qiuming Peng, Tongde Shen, Sulin Zhang[*], Ting Zhu[*] & Jianyu Huang[*]

Table of Contents

Supplementary Methods

Synthesis of arc-discharged CNTs

The CNTs used in this study were prepared by an electrical arcing method. That is, the anode was an asphalt-derived carbon rod, and the cathode was a high-purity graphite electrode (20 mm in diameter, 38 mm in length). To facilitate the collection of CNTs and improve the purity of the CNT samples, we placed a wire net on the top of the two electrodes in the chamber, and the distance between the wire net and the electrodes was about 5 cm. The buffer gas pressure was controlled in the 0.04-0.05 MPa range during the arc discharge experiment. The DC voltage and current for arcing were controlled at 18-20 V and 60-80 A, respectively. The distance between the two electrodes was maintained at about 1-3 mm by manually advancing the anode that was consumed during experiment.

Calculation of cross-sectional area of Li whisker

The as-grown Li whiskers exhibit a variety of growth directions and sizes. To determine the stress in Li whiskers with different orientations and sizes, it is important to accurately measure their cross-section areas. In this experiment, we used two methods to measure the cross-section area of the whisker. One is to rotate the whisker about its longitudinal axis by tilting the sample holder in the axial direction in the ETEM (Supplementary Fig. S25). By observing its projection images from different directions, we can approximately determine the cross-section shape of the whisker and thus its cross-section area. The other method is to push the Li whisker against the AFM tip, such that the whisker was reoriented to expose its cross-section to electron beam (Supplementary Fig. S26). As a result, we can directly measure the cross-section area of the whisker. In addition, to determine the size of a Li whisker, we approximated its cross section as a circle and then obtained the corresponding equivalent diameter as the nominal size of a Li whisker.

Model of Li whisker growth in solid electrolytes

Motivated by the elastic whisker model developed by Porz *et al.*[1], we developed a model of elasto-plastic whisker growth within an elastic solid electrolyte. As schematically illustrated in Supplementary Fig. 24a, we considered the growth of a Li whisker of length a and thickness d ($<< a$) that occupied the open space of a notched main crack of length a in a solid electrolyte. Li atoms were inserted at the interface between the lower end of the whisker and the notch root. The curvature of the notch was ignored, such that the interface was treated as a flat segment. The overpotential at the interface was $\Delta\phi$ and the normal stress at the interface was σ. During Li plating at the interface, $\Delta\phi$ and σ were related according to Eq. (1). The Li whisker was modeled as an elastic-plastic material. Its elastic deformation obeys Hooke's law and plastic deformation obeys the J_2 flow rule. Young's

modulus of the Li whisker was taken as 10 GPa, Poisson's ratio as 0.3, and the yield stress as 200 MPa. The solid electrolyte was modeled as an elastic material. Its Young's modulus was taken as that of $Li_7La_3Zr_2O_{12}$ (LLZO) (150 GPa). Frictional sliding was allowed at the interface between the whisker side face and the solid electrolyte surface. The shear stress σ_{xy} at the interface was related to the local normal stress σ_{xx} by $\sigma_{xy} = \mu\sigma_{xx}$, where the friction coefficient μ was taken as 0.05. The stress distribution within the Li whisker and surrounding solid electrolyte was solved by the finite element method using the commercial package ABAQUS. For the simulation cell in Supplementary Fig. 24b, the cell width was 1.2 μm, the cell height (being equal to a) was 4 μm and the whisker thickness was 200 nm. The finite element calculation was performed under the plane strain condition. The lower end surface of the Li whisker was fixed and other surfaces of the simulation cell was traction free. The upper end surface of the Li whisker was subjected to the prescribed normal stress σ which increased until the lower end of the whisker reached the yield stress of the Li whisker σ_Y. Supplementary Fig. 24b shows the corresponding stress contour of σ_{yy} from the finite element calculation. The corresponding normal stress σ was obtained as $1.1\sigma_Y$, which was higher than the yield stress σ_Y because of the constraining normal stress from the surrounding solid electrolyte and associated frictional shear stress on the side surface of the Li whisker. The calculated normal stress σ (= $1.1\sigma_Y$) was approximately taken as the upper stress limit at the interface between the lower end of the whisker and the notch root of the main crack, which arises due to plastic yielding of the Li whisker. Then we extracted the corresponding normal stress σ_{xx} between the side surface of Li whisker and the crack surface, and used this stress (~$0.34\sigma_Y$) as the representative stress acting on the crack faces for calculating the stress intensity factor of the main crack.

Based on the above finite element simulation of stress generation in an elasto-plastic whisker, we further developed a Li whisker growth map in the parameter space of overpotential $\Delta\phi$ and crack size a in a solid electrolyte of LLZO, as shown in Supplementary Fig. 24c. Specifically, from fracture mechanics, the crack size a and the fracture toughness K_{IC} of the solid electrolyte determine the critical stress σ_c of growth of the main crack at the solid electrolyte surface

$$\sigma_c = K_{IC}/(\gamma\sqrt{\pi a}) \qquad \text{(S1)}$$

where γ is the dimensionless geometric factor of order one for a surface crack, taken as 1.12 (reference 1). For a large crack size a, the critical stress σ_c is relatively low. According to Eq. (1) in the paper, a sufficiently high overpotential $\Delta\phi$ may generate the necessary stress at the lower end of the whisker (being elastic), so as to achieve σ_c for electrolyte fracture. The corresponding critical overpotential $\Delta\phi_c$ can be determined by combining Eq. (S1) and Eq. (1),

$$\Delta\phi_{\mathrm{c}}\gamma\sqrt{\pi a} = K_{\mathrm{IC}}V_{\mathrm{m}}/F \qquad \text{(S2)}$$

which has been given as Eq. (2) in the paper. Eq. (S2) sets the boundary between the domains of "no whisker growth" and "whisker growth" (indicated by the blue solid curve) for large cracks in Supplementary Fig. 24c. On the other hand, Eq. (S1) indicates that a small crack size a corresponds to a high critical stress σ_{c}. However, this critical stress cannot be attained, when the Li whisker is plastically yielded. Hence, Li whisker growth can be entirely suppressed, irrespective of crack size a. The corresponding critical crack size a_{c} can be determined by setting σ_{c} as the upper limit of the crack surface stress ($\sim 0.34\sigma_{\mathrm{Y}}$). This critical crack size determines the boundary between the domains of "no whisker growth" and "whisker growth" (indicated by the vertical blue line) in Fig. 24c. In contrast, for the model of an elastic whisker, the boundary between the domains of "no whisker growth" and "whisker growth" can be determined by extending Eq. (S2) to the small flaw size, as indicated by the white dashed line in Supplementary Fig. 24c. Hence, this map demonstrates the important effect of the elasto-plasticity of Li whisker on its growth behavior under the stiff constraint of solid electrolyte. In addition to the crack growth mechanism studied in this work, other possible mechanisms of Li penetration through solid electrolytes may also play a role, including Li dendrite growth along grain boundaries[2] and in single crystals due to the electric field concentration near the electrode edge[3], as well as electronic conduction through bulk electrolytes[4,5].

Supplementary Discussion

The relationship between stress and overpotential

(1) *Non-linear vs linear relationship between overpotential and current*

As a Li whisker grows, the Li ionic current is influenced by both overpotential and stress. As schematically shown in Supplementary Fig. 20a, the growing Li whisker, Li_2CO_3 electrolyte layer and Li metal substrate form a symmetric battery cell, with Li metal on both sides of the electrodes. Under an overpotential $\Delta\phi$, Li ions leave the Li metal substrate, diffuse through the Li_2CO_3 electrolyte and deposit at the contact interface between the Li whisker and the Li_2CO_3 surface. Meanwhile, the reverse process also occurs, such that Li ions are extracted from the contact interface and move back to the Li metal substrate. In addition to an overpotential, the Li whisker is subjected to an axial compressive stress σ (being positive for compression). Hence, the electrical and mechanical coupling manifests through their respective work on the Li insertion process at the contact interface. Namely, the Li insertion is aided by the electrical work $F\Delta\phi$ (F being the Faraday constant) done by the overpotential, but is opposed by the mechanical work σV_m done by the stress; here V_m is the Li molar volume, which is equivalent to the volume per Li ion if F is taken as the charge per Li ion. As a result, the net Li current density i at the contact interface can be expressed by a modified Butler-Volmer equation of the form

$$i = i_0 \exp\left[\frac{\alpha(F\Delta\phi - \sigma V_\mathrm{m})}{RT}\right] - i_0 \exp\left[-\frac{(1-\alpha)(F\Delta\phi - \sigma V_\mathrm{m})}{RT}\right] \qquad \text{(R1)}$$

where i_0 is the exchange current density, α is the charge transfer coefficient (taken as ½ for simplicity), R is the universal gas constant and T is the temperature. On the right side of Eq. (R1), the first term gives the rate of Li deposition at the contact interface, and $F\Delta\phi - \sigma V_m$ represents the effects of electrical and mechanical work during Li deposition. The second term gives the rate of Li extraction from the contact interface, and $-(F\Delta\phi - \sigma V_\mathrm{m})$ represents the effects of electrical and mechanical work during Li extraction. It is seen from Eq. (R1) that the Li ion current and overpotential generally do not follow a linear relationship. When $F\Delta\phi > \sigma V_\mathrm{m}$, Eq. (1) shows that a net Li current density is positive, causing the growth of the Li whisker. When σV_m is increased to become sufficiently close to $F\Delta\phi$ and thus $F\Delta\phi - \sigma V_\mathrm{m}$ becomes much smaller than RT, one can use Taylor's expansion (i.e., $\exp(x) = x$ when $x << 1$) to linearize Eq. (R1) as

$$i = i_0 \left(\frac{F\Delta\phi - \sigma V_\mathrm{m}}{RT}\right) \qquad \text{(R2)}$$

Eq. (R2) gives an approximately linear relationship between overpotential and Li current. However, we note that under a given overpotential $\Delta\phi$, the stress σ can increase with the

increasing length l of the Li whisker, causing time-dependent changes of the Li ion current i even when Eq. (R2) holds. Hence, strictly speaking, there is no linear relationship between overpotential and Li current for both the large and small current density i.

To summarize, Eq. (R1) shows that the Li ion current and overpotential generally do not follow a linear relationship; and Eq. (R2) shows that an approximately linear relationship can be achieved, when $F\Delta\phi - \sigma V_{\mathrm{m}}$ approaches zero and thus i becomes small (i.e., the growth of the Li whisker nearly stops under a given overpotential $\Delta\phi$).

(2) *Linear relationship between overpotential and the corresponding critical stress when the growth of a Li whisker stops*

To understand Eq. (1) in the text that presents a linear relationship between overpotential and stress, we must first clarify the definition of the stress in this equation. That is, under an overpotential $\Delta\phi$, the stress in Eq. (1) is the critical stress when the growth of the Li whisker stops. In Supplementary Fig. 20b, we show the case when the growth of a Li whisker stops under a given overpotential $\Delta\phi_1$. The corresponding critical stress is σ_1 and the corresponding critical length of the Li whisker is l_1. In this case, the net Li ion current is zero. Hence, according to Eq. (R1) and (R2), the following condition is satisfied: $F\Delta\phi_1 = \sigma_1 V_{\mathrm{m}}$, which corresponds to an energy balance between the electrical work and mechanical work associated with Li insertion/extraction at the contact interface. In Supplementary Fig. 20c, the overpotential is increased to $\Delta\phi_2$. The Li whisker resumes its growth. As the Li whisker length increases from l_1 to l, the compressive stress increases from σ_1 to σ. Correspondingly, $F\Delta\phi_2 > \sigma V_{\mathrm{m}}$ and the net Li current is positive. This growth process continues until a new energy balance is satisfied. As shown in Supplementary Fig. 20d, the growth of the Li whisker stops under the overpotential $\Delta\phi_2$. The corresponding critical stress is σ_2 and the corresponding length of the Li whisker is l_2. Likewise, according to Eq. (R1) and (R2), the following work balance condition is satisfied: $F\Delta\phi_2 = \sigma_2 V_{\mathrm{m}}$.

Based on the above discussion, it is necessary to distinguish the critical compressive stress (denoted as $\tilde{\sigma}$) with the general compressive stress (denoted as σ) in the Li whisker. Hence, we rewrite equation (1) as

$$\tilde{\sigma} V_{\mathrm{m}} = F\Delta\phi \qquad \text{(R3)}$$

As such, the stress $\tilde{\sigma}$ has a one-to-one linear relation with the overpotential $\Delta\phi$, giving a constitutive equation between $\Delta\phi$ and $\tilde{\sigma}$ when the growth of the Li whisker stops. The energy balance relation in Eq. (R3) gives rise to zero Li current i in both Eqs. (R1) and

R(2). Hence, the linear relationship between overpotential $\Delta\phi$ and stress $\tilde{\sigma}$ does not require a linear relationship between overpotential and current.

(3) *Potential partition in the testing system and the relationship between the applied voltage and the corresponding critical stress when the growth of a Li whisker stops*

To understand the voltage partition throughout the testing system (as schematically shown in Supplementary Fig. 21a), we draw its equivalent circuit in Supplementary Fig. 21b. Here, R_1 represents the effective Ohm resistance of the AFM part (enclosed by the blue circle in Supplementary Fig. 21a); R_2 represents the effective Ohm resistance associated with an electronic conduction path through the combined Li whisker and Li_2CO_3/Li metal (enclosed by the green circle in Supplementary Fig. 21a); and R_3 represents the effective charge transfer resistance of the ionic conduction path (also enclosed by the green circle in Supplementary Fig. 21a). Compared with R_1, R_2 and R_3, both the Li whisker and Li metal substrate can be reasonably assumed to have much lower electrical resistances. The electrical current I in the system corresponds to the electron current I'_{e} in R_1, as well as the sum of the electron current I''_{e} in R_2 and the Li current I_i in R_3. The voltage over R_3 is the overpotential $\Delta\phi$ driving Li deposition at the contact interface. Our experimental measurements indicate that there is a very large threshold voltage (~ 5V) that has to be overcome to initiate Li growth, and this threshold voltage (denoted as ϕ_{a0}) can be mainly attributed to the non-Ohm contact resistance between the AFM tip (composed of a Si tip covered with a native SiO_2 surface layer) and the Li whisker. During the growth of a Li whisker, the applied voltage ϕ_{a}, overpotential $\Delta\phi$ and stress σ are generally related to each other in a non-linear manner through the following set of equations

$$I'_{\mathrm{e}} = I_{\mathrm{i}} + I''_{\mathrm{e}},\ I'_{\mathrm{e}} = (\phi_{\mathrm{a}} - \phi_{\mathrm{a0}} - \Delta\phi)/R_1 \qquad \text{(R4)}$$

$$I''_{\mathrm{e}} = \Delta\phi/R_2,\ I_{\mathrm{i}} = Ai_0 \exp\left[\frac{\alpha(F\Delta\phi - \sigma V_{\mathrm{m}})}{RT}\right] - Ai_0 \exp\left[-\frac{(1-\alpha)(F\Delta\phi - \sigma V_{\mathrm{m}})}{RT}\right]$$

where A is the contact area between the Li whisker and the surface of the Li_2CO_3/Li metal substrate. Under an applied voltage ϕ_a, the stress σ increases and the Li ion current I_{i} decreases with the increasing length of the growing Li whisker. As I_i becomes very small the linearized Eq. (R2) can be used to relate I_i and $\Delta\phi$. Then we rewrite Eq. (R2) as $I_{\mathrm{i}} = (\Delta\phi - \sigma V_{\mathrm{m}}/F)/R_3$, where the effective charge transfer resistance R_3 is given by $R_3 = RT/(i_0 FA)$. It follows that Eqs. (R4) can be simplified as

$$I'_{\mathrm{e}} = I_{\mathrm{i}} + I''_{\mathrm{e}}, I'_{\mathrm{e}} = (\phi_{\mathrm{a}} - \phi_{\mathrm{a0}} - \Delta\phi)/R_1, I''_{\mathrm{e}} = \Delta\phi/R_2, I_{\mathrm{i}} = (\Delta\phi - \sigma V_{\mathrm{m}}/F)/R_3 \qquad \text{(R5)}$$

In Fig. 2d, we show the experimental data of the applied voltage ϕ_{a} versus the corresponding critical stress $\tilde{\sigma}$ when a Li whisker stops its growth, i.e., $I_{\mathrm{i}} = 0$. Hence, to establish a functional relationship between ϕ_{a} and $\tilde{\sigma}$, we only need to consider the limit of zero ionic current ($I_{\mathrm{i}} = 0$) under different ϕ_{a}. When $I_{\mathrm{i}} = 0$, $I'_{\mathrm{e}} = I''_{\mathrm{e}}$. Then we can combine $I'_{\mathrm{e}} = (\phi_{\mathrm{a}} - \phi_{\mathrm{a0}} - \Delta\phi)/R_1$ and $I''_{\mathrm{e}} = \Delta\phi/R_2$ to eliminate $\Delta\phi$, so as to obtain $I'_{\mathrm{e}} = I''_{\mathrm{e}} = (\phi_{\mathrm{a}} - \phi_{\mathrm{a0}})/(R_1 + R_2)$. It follows that the corresponding overpotential $\Delta\phi$ is given by $\Delta\phi = R_2 I''_{\mathrm{e}} = R_2(\phi_{\mathrm{a}} - \phi_{\mathrm{a0}})/(R_1 + R_2)$ and can be rewritten as

$$\Delta\phi = r(\phi_{\mathrm{a}} - \phi_{\mathrm{a0}}) \tag{R6}$$

where $r \equiv R_2/(R_1 + R_2)$. Combination of Eq. (R3) and (R6) yields a one-to-one relation between the applied voltage ϕ_{a} and corresponding critical stress $\tilde{\sigma}$ when the growth of the Li whisker stops,

$$\tilde{\sigma} = \frac{F}{V_{\mathrm{m}}}\Delta\phi = \frac{F}{V_{\mathrm{m}}} r(\phi_{\mathrm{a}} - \phi_{\mathrm{a0}}) \tag{R7}$$

Note that due to the possible changes of R_1, R_2 and accordingly r as a Li whisker grows, Eq. (R6) does not necessarily suggest a linear relationship between the overpotential and the applied voltage, neither Eq. (R7) suggests a linear relationship between the measured stress $\tilde{\sigma}$ and applied voltage ϕ_{a}. However, this part of analysis provides an understanding of how the applied voltage is related to the overpotential through Eq. (R6) and to the stress through Eq. (R7).

Supplementary Movies

Supplementary Movie 1 An *in situ* TEM movie showing the growth of a Li whisker (corresponding to **Figure 1d**). As a negative potential was applied to the CNT against Li, a single Li spheroid started to nucleate at the contact point between the CNT and the Li_2CO_3 on the surface of the Li metal and then grew along the CNT, pushing the AFM cantilever upward. As the Li ball grew to about 1.26 μm in size, a whisker emerged underneath the ball which pushed the AFM cantilever up, thus generating the axially compressive stress in the whisker. When the whisker reached 4.08 μm in length, it collapsed due to the compression by the AFM tip. The attachment of a CNT to the AFM tip rendered controllable whisker nucleation. The movie was recorded at 5 frames/second in the bright field (BF) mode, and played at 97× speed (during ball generation) and 49× speed (during Li whisker generation).

Supplementary Movie 2 An *in situ* TEM movie showing the growth of a Li whisker (corresponding to **Supplementary Fig. 3**). The Li whisker grows directly underneath the AFM cantilever without the prior formation of Li balls. The movie was recorded at 5 frames/second in BF mode, and played at 5× speed.

Supplementary Movie 3 A Li whisker grows directly underneath the AFM cantilever (corresponding to **Supplementary Fig. 4**). A Li ball grows prior to the growth of a whisker. The movie was recorded at 5 frames/second in BF mode, and played at 212× speed (during ball generation) and 157× speed (during Li whisker generation).

Supplementary Movie 4 A Li whisker grows directly underneath the AFM cantilever (corresponding to **Supplementary Fig. 5**). The movie was recorded at 5 frames/second in the BF mode, and played at 61× speed (during ball generation) and 44× speed (during Li whisker generation).

Supplementary Movie 5 An *in situ* TEM movie showing the growth of a Li whisker underneath the AFM cantilever (corresponding to **Supplementary Fig. 6**). The whisker buckles after reaching a length of 1.90 μm. The movie was recorded at 5 frames/second in BF mode, and played at 13× speed (during ball generation) and 10× speed (during Li whisker generation).

Supplementary Movie 6 An *in situ* TEM movie showing the growth of a Li whisker underneath the AFM cantilever (corresponding to **Supplementary Fig. 7**). The movie was recorded at 5 frames/second in BF mode, and played at 8× speed.

Supplementary Movie 7 An *in situ* TEM movie showing the growth of a Li whisker underneath the AFM cantilever (corresponding to **Supplementary Fig. 8**). The movie was recorded at 5 frames/second in BF mode, and played at 184× speed.

Supplementary Movie 8 An *in situ* TEM movie showing the growth of a Li whisker with <001> orientation (corresponding to **Supplementary Fig. 12**). A Li ball forms prior to the whisker growth. The movie was recorded at 5 frames/second in BF mode, and played at 188×speed (during ball generation) and 156× speed (during Li whisker generation).

Supplementary Movie 9 An *in situ* TEM movie showing the growth of a Li whisker with <112> orientation (corresponding to **Supplementary Fig. 13**). The movie was recorded at 5 frames/second in BF mode, and played at 15× speed.

Supplementary Movie 10 An *in situ* TEM movie showing the growth of a Li whisker with <110> orientation (corresponding to **Supplementary Fig. 14**). The movie was recorded at 5 frames/second in BF mode, and played at 31× speed (during ball generation) and 22× speed (during Li whisker generation).

Supplementary Movie 11 An *in situ* TEM movie showing the growth of a Li whisker with <111> orientation (corresponding to **Supplementary Fig. 15**). The movie was recorded at 5 frames/second in BF mode, and played at 51× speed.

Supplementary Movie 12 An *in situ* TEM movie showing the growth of a Li ball at the CNT and Li_2CO_3 contact point (corresponding to **Supplementary Fig. 16**). The movie was recorded at 5 frames/second in BF mode, and played at 201× speed.

Supplementary Movie 13 An *in situ* TEM movie showing the generation of a Li whisker (corresponding to **Figure 2a**). A faceted Li nanocrystal formed prior to the formation of a Li whisker. The movie was recorded at 5 frames/second in BF mode, and played at 46× speed (during ball generation) and 25× speed (during Li whisker generation).

Supplementary Movie 14 An *in situ* TEM movie showing the growth of a Li whisker. In order to explore the relationship between the applied voltage and the growth stress, the potential was ramped up after the Li whisker ceased its growth (corresponding to **Supplementary Fig. 18**), which stimulated further whisker growth. The movie was recorded at 5 frames/second in BF mode, and played at 24× speed.

Supplementary Movie 15 An *in situ* TEM movie showing the growth of a Li whisker. In order to explore the relationship between the applied voltage and the growth stress, the potential was ramped up after the Li whisker ceased its growth, which stimulated further whisker growth (corresponding to **Supplementary Fig. 19**). The movie was recorded at 5 frames/second in BF mode, and played at 18× speed.

Supplementary Movie 16 An *in situ* TEM movie showing the growth of a Li whisker. In order to explore the relationship between the applied voltage and the growth stress, the potential was ramped up after the Li whisker ceased its growth (corresponding to **Supplementary Fig. 2c**). The movie was recorded at 5 frames/second in BF mode, and played at 25× speed.

Supplementary Movie 17 Assessing the mechanical properties of a Li whisker by *in situ* compression (corresponding to **Supplementary Fig. 22**). After its growth, the whisker was pushed up against the AFM cantilever, causing the whisker to deform. The movie was recorded at 5 frames/second in BF mode, and played at 14× speed.

Supplementary Movie 18 *In situ* growth followed by *in situ* compression of a Li whisker. (corresponding to **Supplementary Fig. 23**). The whisker was manipulated to contact the AFM tip, causing growth of a secondary whisker over the old one at the bottom, pushing up against the AFM tip under bias. The movie was recorded at 5 frames/second in BF mode, and played at 48× speed.

Supplementary Movie 19 Assessing the mechanical properties of a Li whisker by *in situ* compression (corresponding to **Supplementary Fig. 26**). After its growth, the whisker was pushed up against the AFM cantilever, causing the whisker to deform. The movie was recorded at 5 frames/second in BF mode, and played at 18× speed.

Supplementary Figures

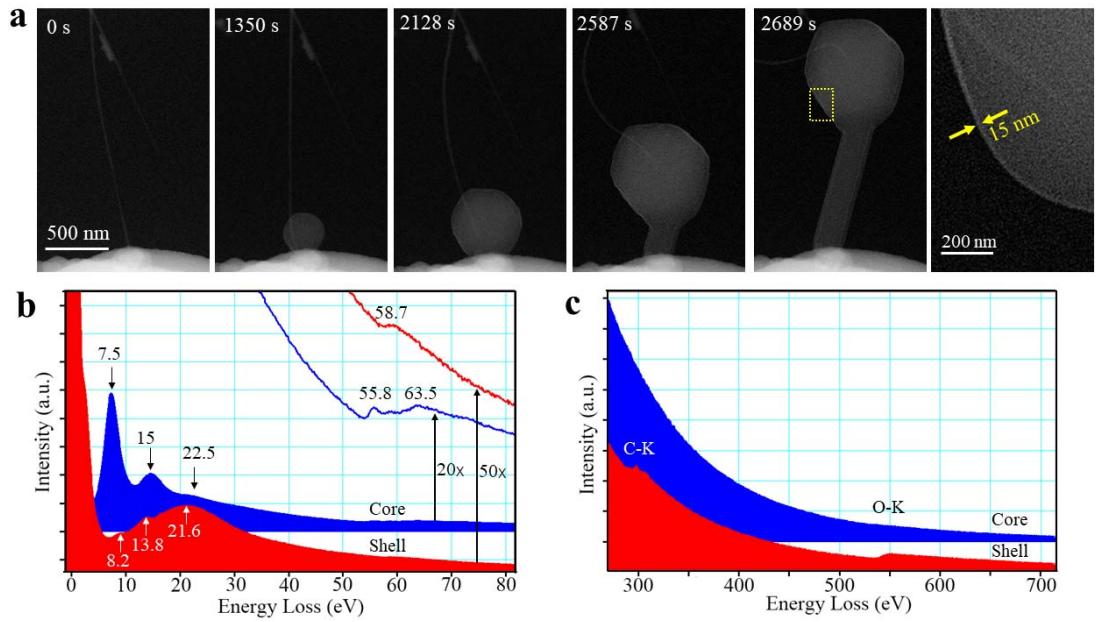

Figure 1 | (c.f. Supplementary Fig. 10) The growth of Li whisker was facilitated by the formation of Li_2CO_3 surface layer. a, Time-lapse TEM images of the Li whisker growth under annular dark field (ADF) mode. **b**, **c,** Low-loss and core-loss EELS spectra from the core and shell of the Li whisker. The EELS profile is consistent with that of Li (blue plot) and Li_2CO_3 (red plot), respectively, which is also consistent with our previous investigation[6].

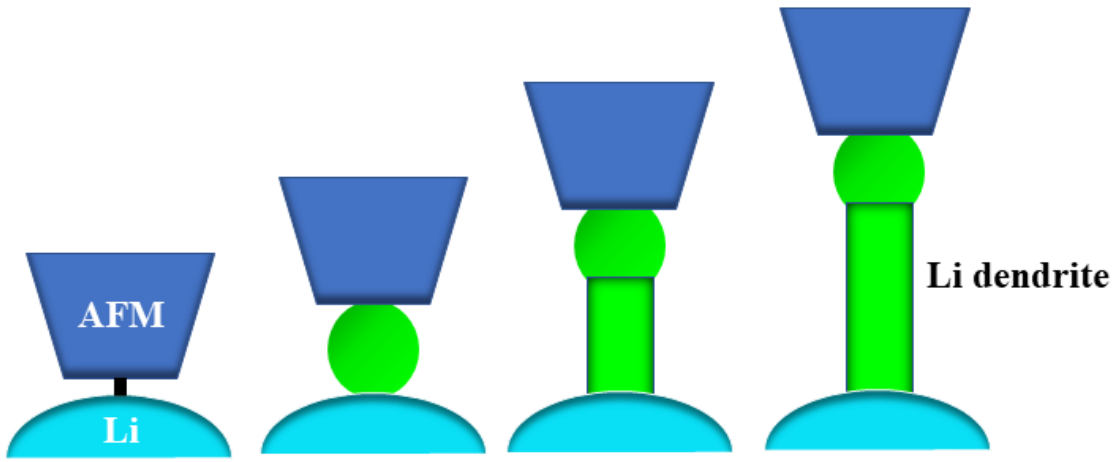

Figure 2 | Schematic of the experimental setup and the whisker growth process.

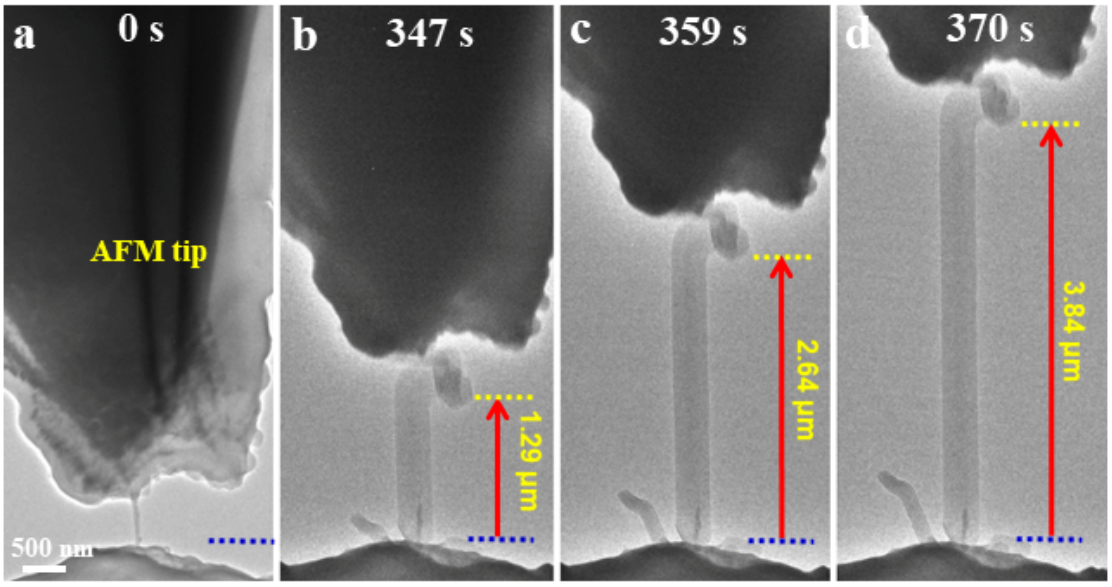

Figure 3 | *In situ* TEM imaging the stress generation during the Li whisker growth. a-d, The Li whisker growth initiated from the CNT and Li_2CO_3 contact point, grew straight upward, pushing up the AFM tip (k=0.1 N/m), generating an opposing stress in the whisker.

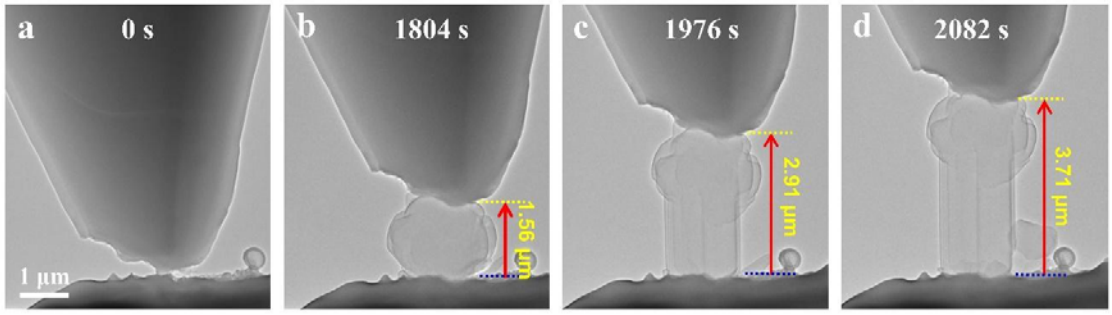

Figure 4 | Sequential TEM images showing the whisker growth process (k=0.1 N/m).

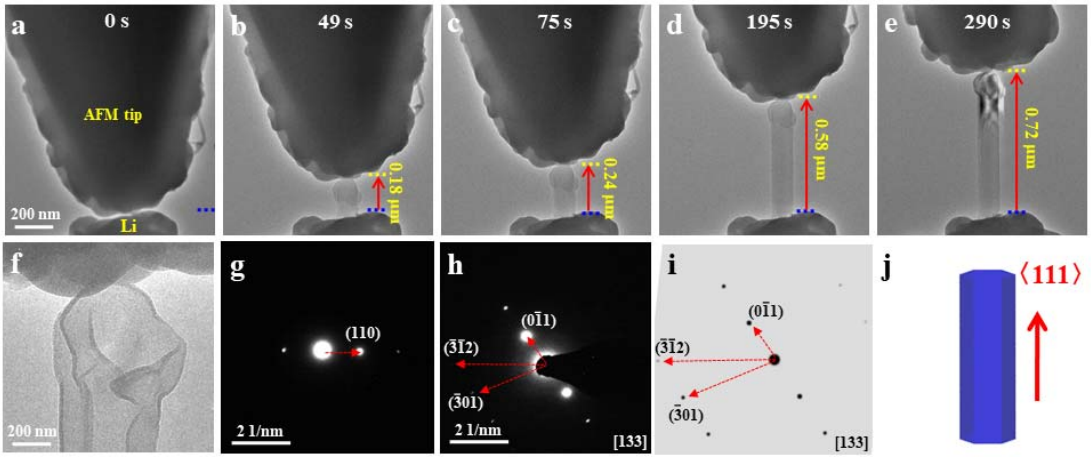

Figure 5 | a-e, Sequential TEM images showing the whisker growth process, which initiated from the growth of a Li ball underneath the AFM tip (49 s) (*k*=0.1 N/m). When the ball grew to about 0.18 μm, it necked down to form a whisker (75 s, 195 s, 290 s). **f-j**, The growth direction of the whisker is <111>, and its cross-section is hexagonal.

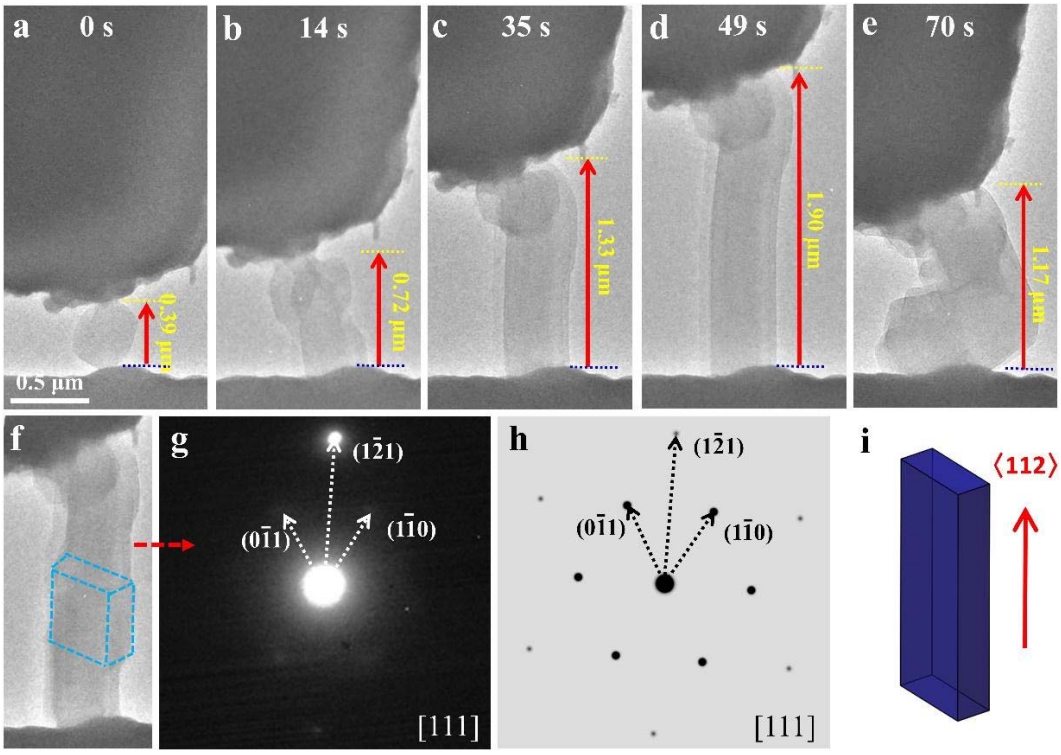

Figure 6 | a-e, Sequential TEM images showing the whisker growth process, which initiated from the growth of a Li ball underneath the AFM tip (a) (*k*=6 N/m). When the ball grew to about 0.39 μm (a), it necked down to form a whisker (b-d), which collapsed after it reached a length of 1.90 μm. **f-i**, The growth direction of the whisker is <112>, and its cross-section is rectangular.

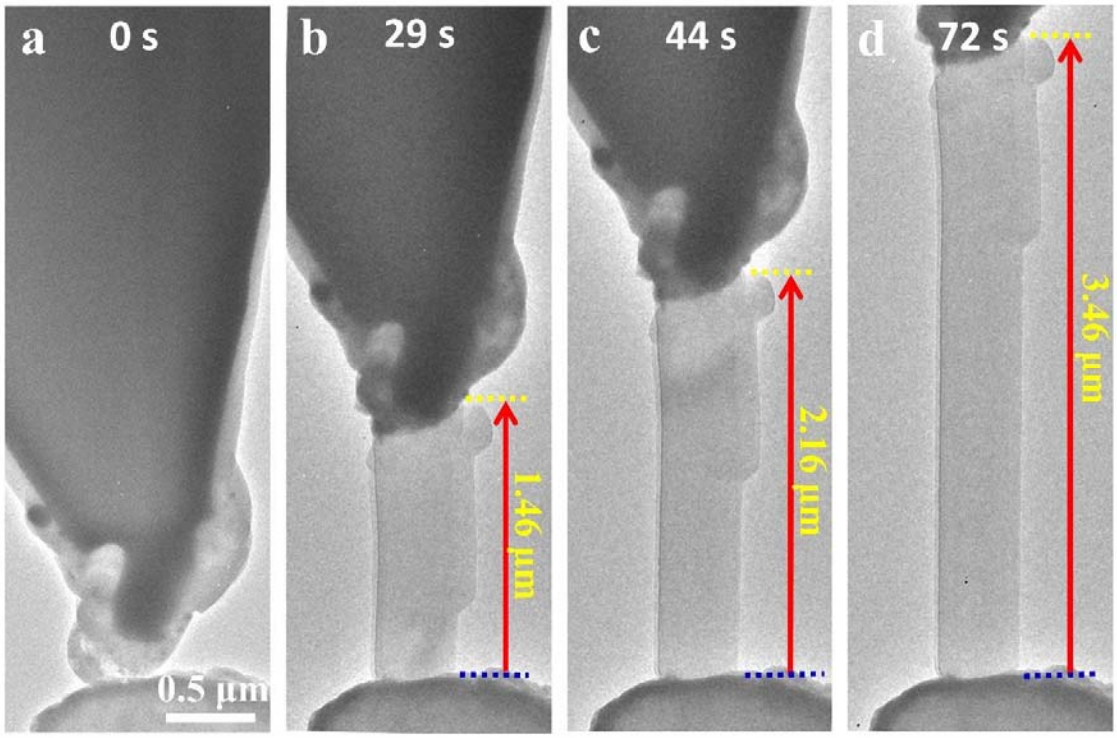

Figure 7 | Sequential TEM images showing the growth of a Li whisker underneath an AFM tip (*k*=0.1 N/m).

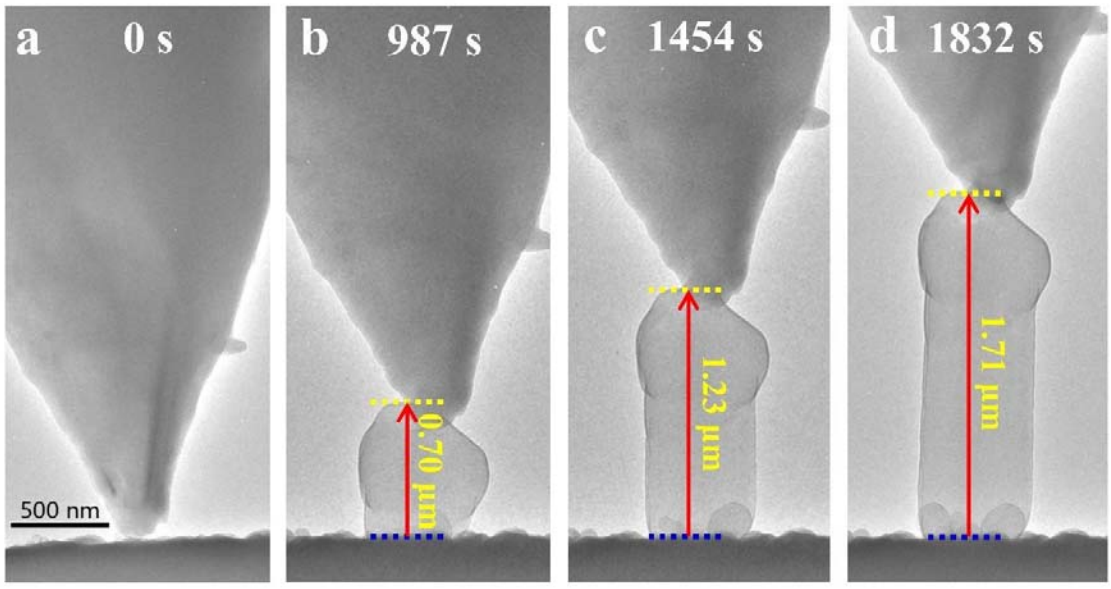

Figure 8 | Sequential TEM images showing the growth of a Li whisker underneath an AFM tip (*k*=0.4 N/m).

Figure 9 | The growth of mushroom
(https://www.bilibili.com/video/av37919832?from=search&seid=17306397480649468019).

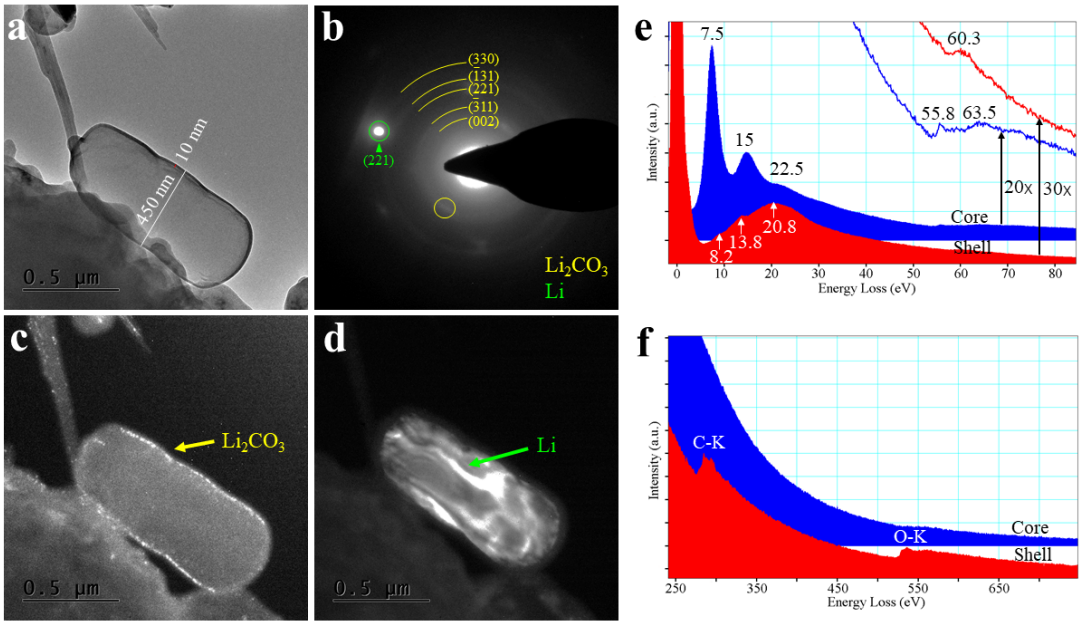

Figure 10 | Electron microscopy characterization of the Li whisker showing the formation of Li_2CO_3 surface layer. a, TEM images of the as grown Li whisker with a diameter of 450 nm, with a Li_2CO_3 shell layer of 10 nm. **b**, The related selected area electron diffraction (SAED) pattern of the Li whisker. The diffraction rings are indexed as Li_2CO_3, and the bright sharp diffraction spot is indexed as Li. **c**, **d**, The dark field images formed by selecting a portion of the diffraction rings (yellow circle) and the sharp diffraction spots (green circle) in (b), respectively, showing the surface layer being Li_2CO_3 (c), and the core being Li (d). **e**, Low-loss EELS spectra from the core and shell of the Li whisker agree excellently with that of Li (blue profile) and Li_2CO_3 (red profile), respectively. **f**, In the core-loss spectra, the core of the Li whisker shows no traces of C and O, while that from the shell region consistently shows the presence of C and O.

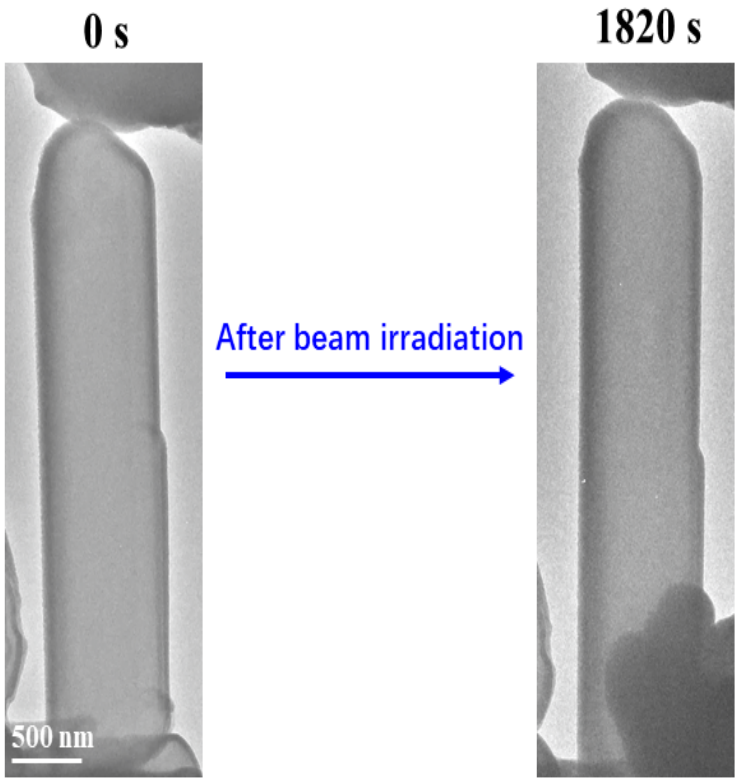

Figure 11 | A whisker was exposed to ebeam irradiation for 1820 s, showing no discernible irradiation damage to the Li whisker due to protection of the surface Li_2CO_3 layer.

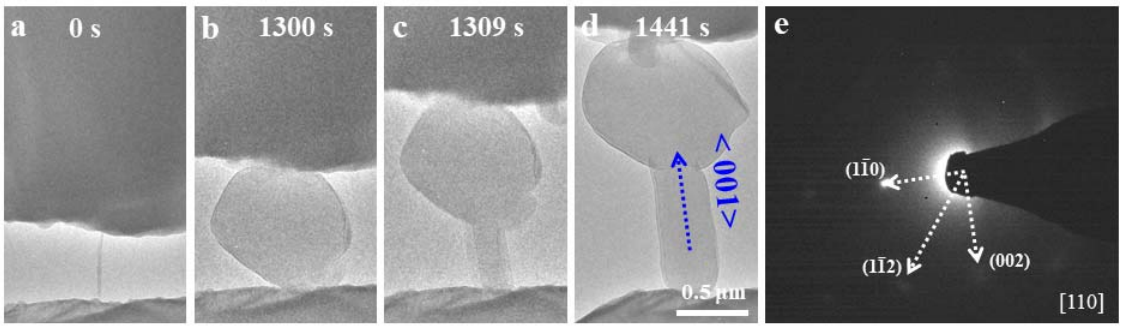

Figure 12 | Sequential TEM images showing the growth of a Li whisker underneath an AFM tip with the growth direction being <001> (*k*=2 N/m).

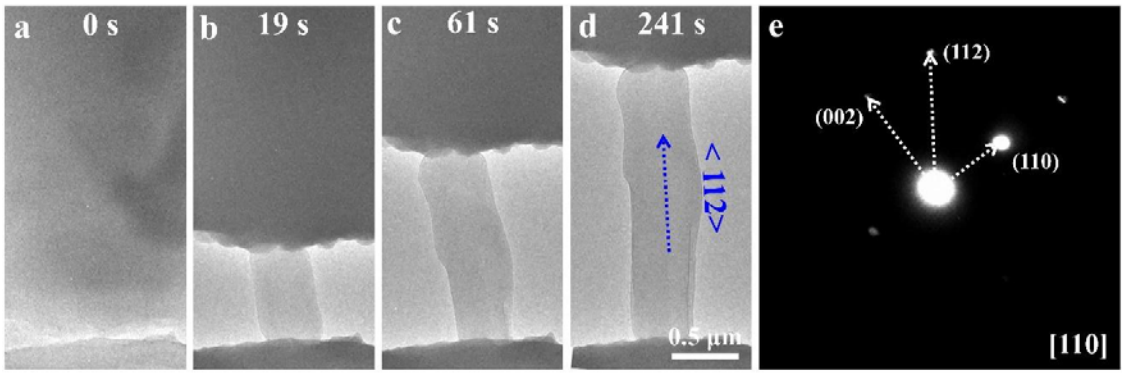

Figure 13 | Sequential TEM images showing the growth of a Li whisker underneath an AFM tip with the growth direction being <112> (*k*=6 N/m).

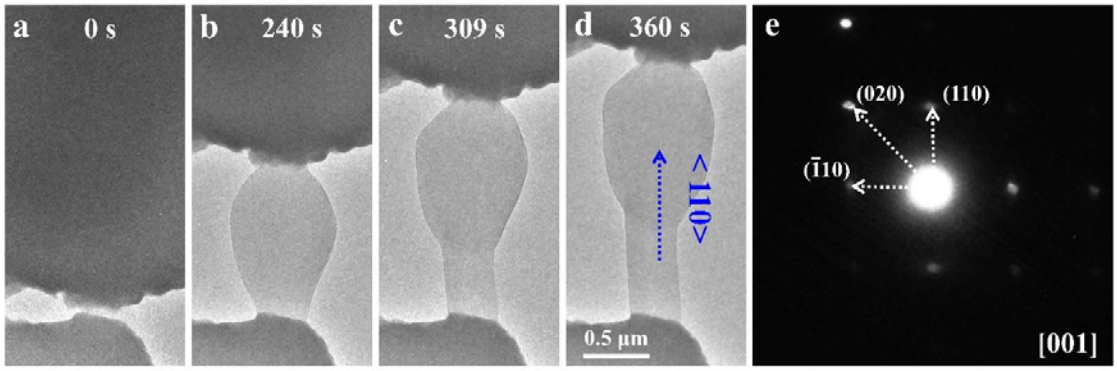

Figure 14 | Sequential TEM images showing the growth of a Li whisker underneath an AFM tip with the growth direction being <110> (*k*=6 N/m).

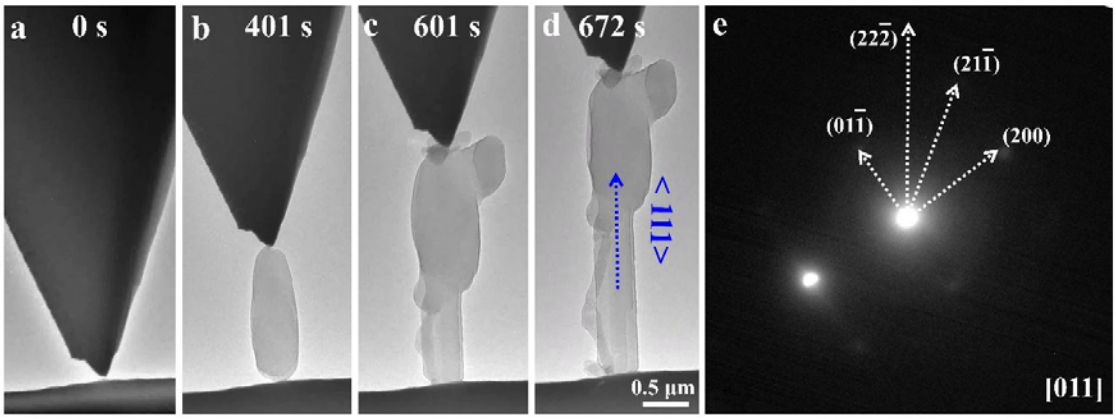

Figure 15 | Sequential TEM images showing the growth of a Li whisker underneath an AFM tip with the growth direction being <111> (*k*=0.1 N/m).

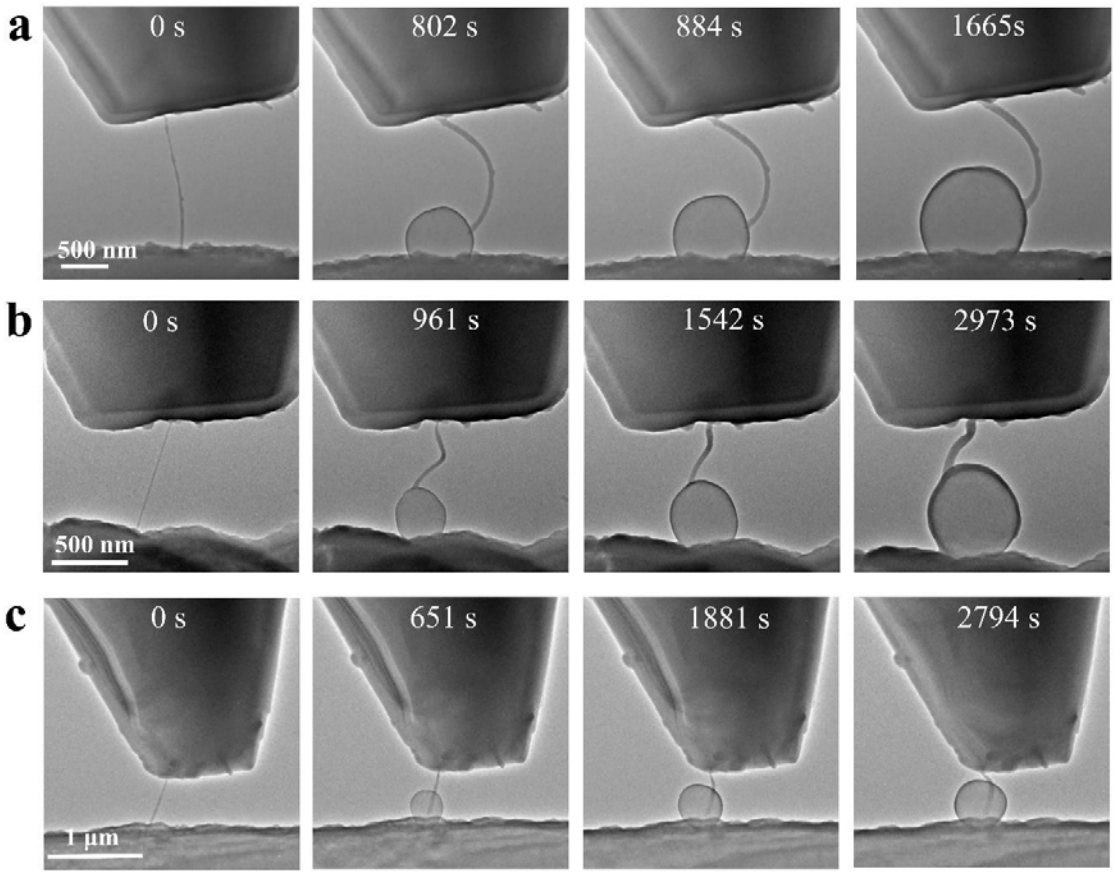

Figure 16 | Growth of Li balls. **a-c**, Three sets of sequential TEM images showing the growth of Li balls at the CNT and Li_2CO_3 contact points.

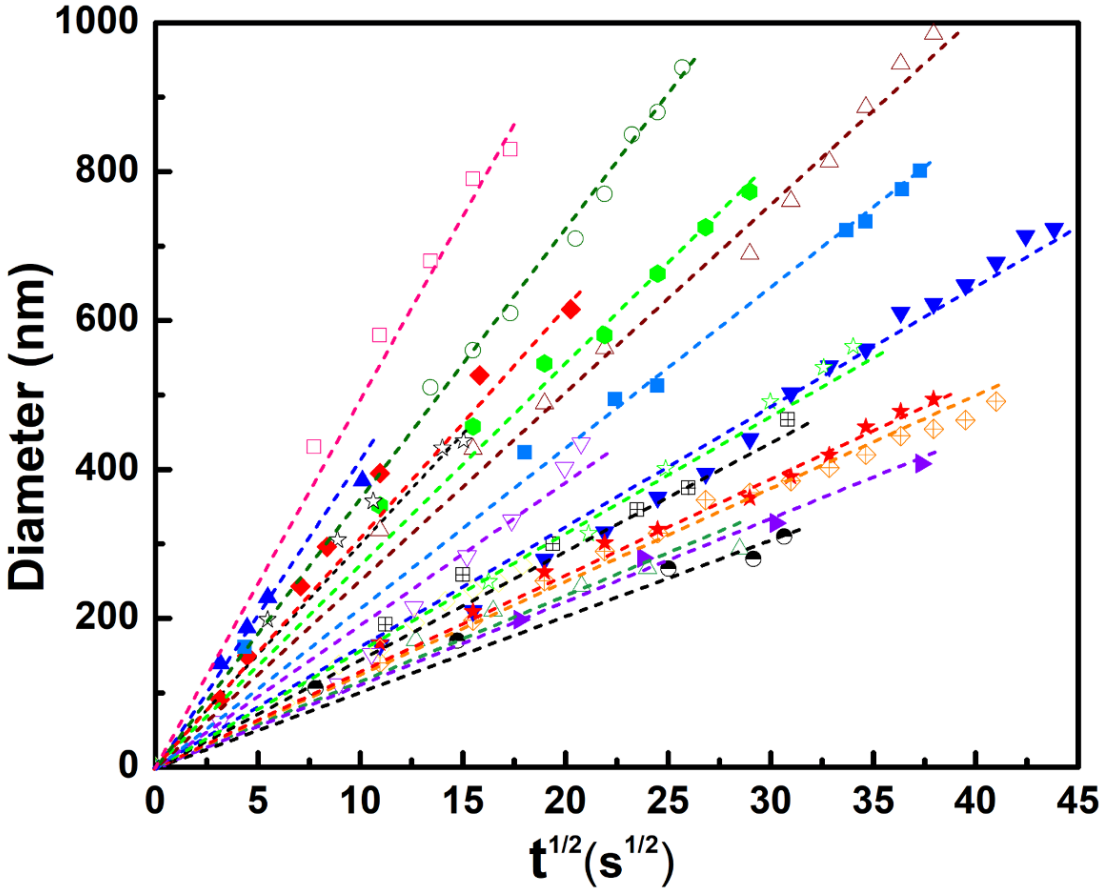

Figure 17 | The diameter of the Li balls such as those shown Supplementary Fig. 16 follows a square-root relationship with growth time, indicating a diffusion-controlled Li ball growth process.

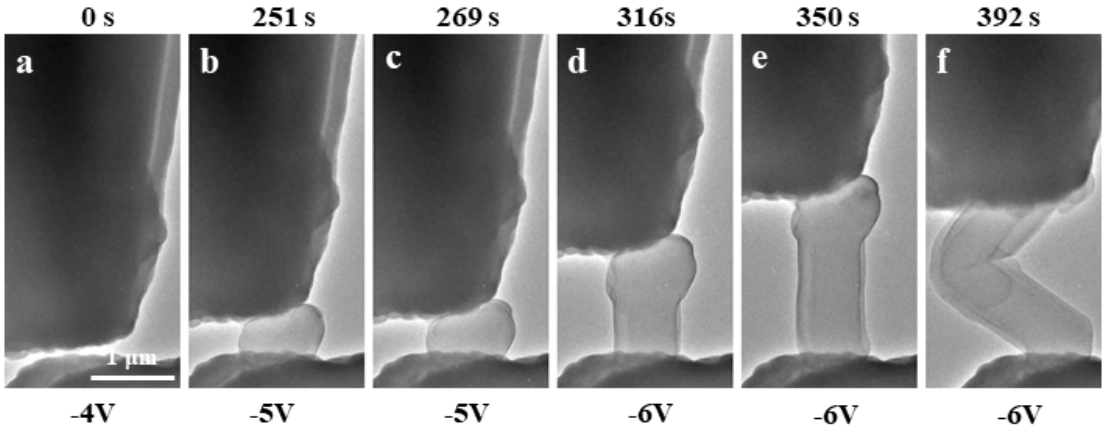

Figure 18 | TEM images showing the stress increasing with overpotential. a-c, Under certain applied voltage, the whisker ceased its growth. **c-e**, Upon increasing the voltage, the whisker resumed its growth. **f,** After growing to certain length, the stress in the whisker reached its maximum growth stress, when the whisker collapsed (k=3 N/m).

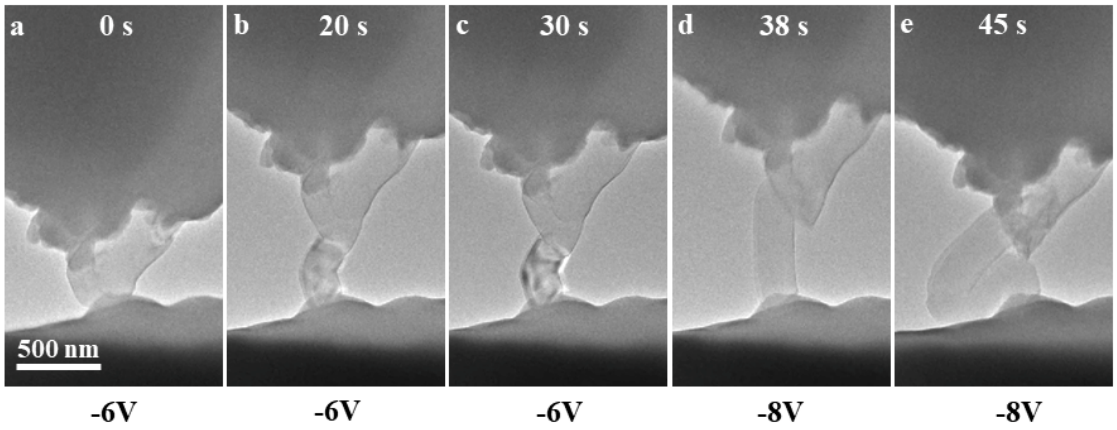

Figure 19 | TEM images showing the stress increasing with applied voltage. a-c, Under certain applied voltage, the whisker ceased its growth; **c-d**, upon increasing the voltage, the whisker resumed its growth. **e,** After growing to certain length, the stress in the whisker reached its maximum growth stress, when the whisker collapsed (k=3 N/m).

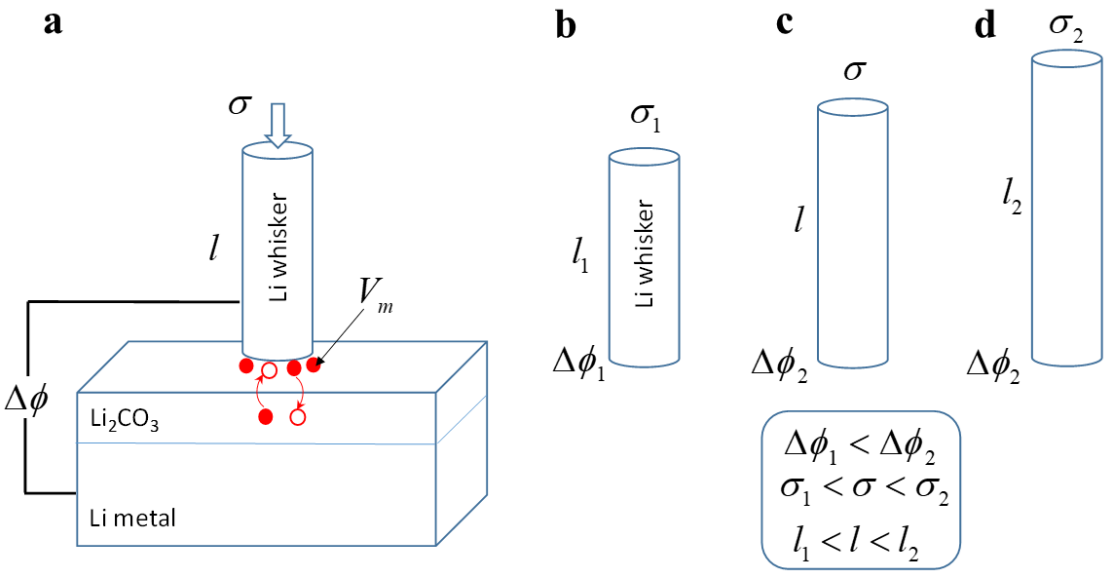

Figure 20 | Schematic illustration of the relationship between overpotential and stress during the growth of a Li whisker. a, Under the overpotential $\Delta\phi$ and compressive stress σ, the growth of a Li whisker results from a higher rate of Li ion insertion (e.g., from a red solid circle to a hollow one) than extraction (e.g., from a red solid circle to a hollow one) at the contact interface between the Li whisker and the Li_2CO_3 surface. **b**, Under the overpotential $\Delta\phi_1$, the growth of the Li whisker stops when a sufficiently high stress is built up; this critical stress is σ_1 and the corresponding Li whisker length is l_1. **c**, When the overpotential is increased to $\Delta\phi_2$, the Li whisker resumes its growth. As the Li whisker length increases from l_1 to l, the compressive stress increases from σ_1 to σ. **d**, Under the overpotential $\Delta\phi_2$, the growth of the Li whisker stops again, when the stress increases to the critical stress σ_2 and the corresponding Li whisker length is l_2.

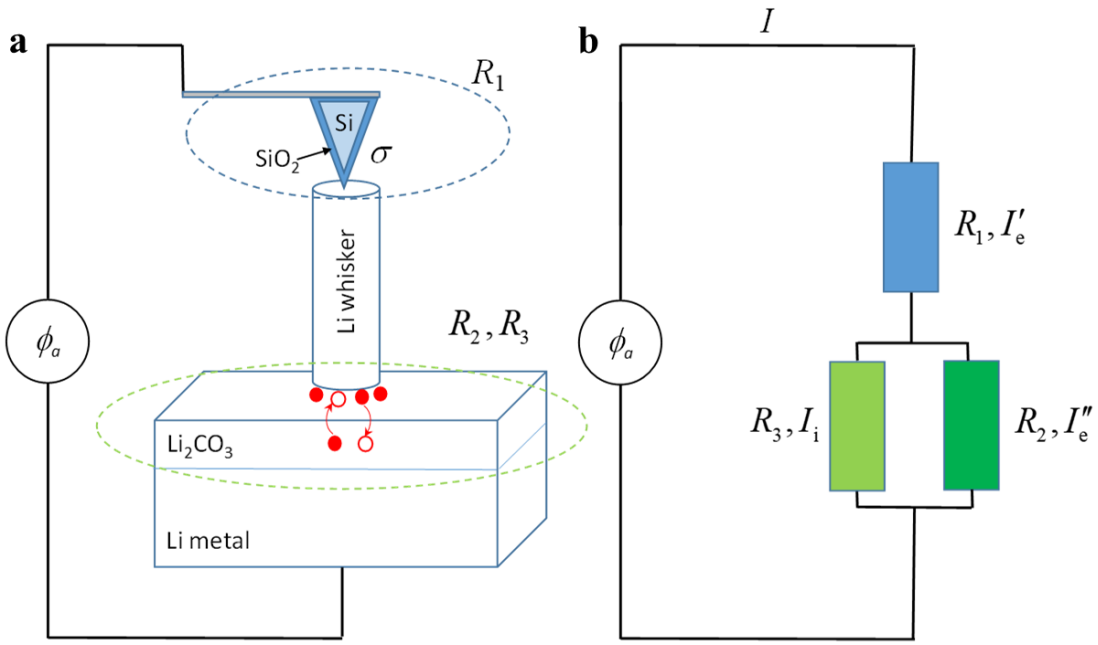

Figure 21 | Analysis of voltage partition and current flow in the testing system. a, Schematic of growth of a Li whisker in the testing system. Under the applied potential ϕ_a and the growth-induced axial compressive stress σ, Li ions can be inserted and extracted concurrently at the interface between the Li whisker and Li_2CO_3/Li metal substrate. A positive net Li ion current results in growth of the Li whisker. **b**, The equivalent circuit of the testing system in (a).

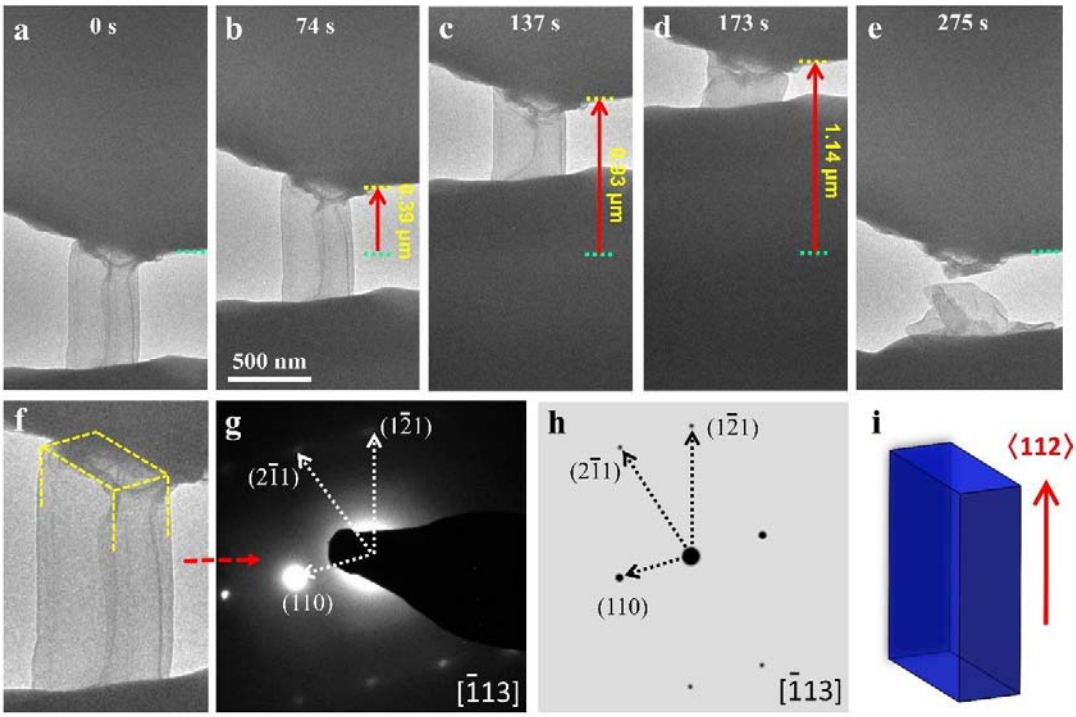

Figure 22 | *In situ* compression of an as-grown Li whisker. The whisker was manipulated to contact the AFM tip (**a**), which was pushed up against the AFM tip (**b-d**) (*k*=6 N/m). Red arrowheads mark the displacement of the AFM tip. The whisker collapsed after extensive compression (**d**). The cross-section of the whisker is rectangular (**f**), and its growth direction is [112] (**g-i**).

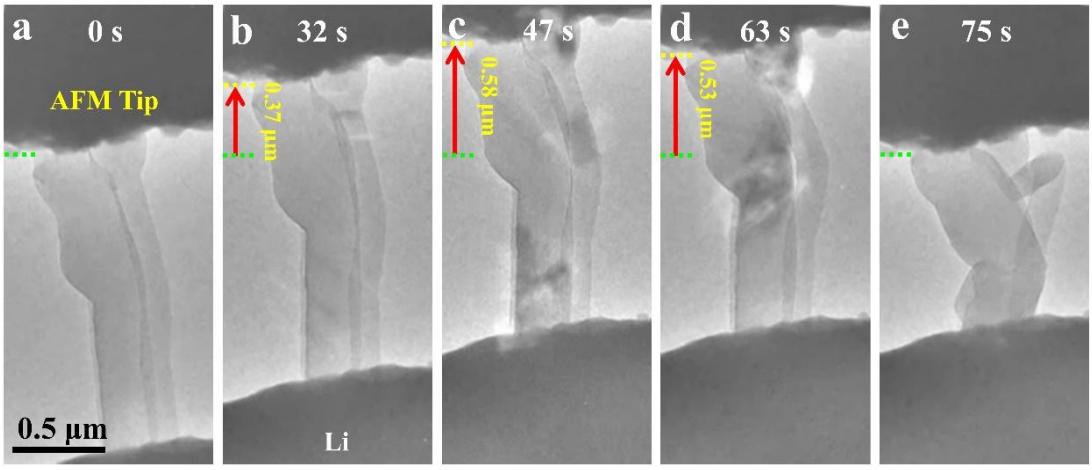

Figure 23 | *In situ* compression of an as-grown Li whisker. The whisker was manipulated to contact the AFM tip (**a**), which was pushed up against the AFM tip (**b-d**) (*k*=6 N/m). Red arrowheads mark the displacement of the AFM tip. The whisker collapsed after extensive compression (**e**).

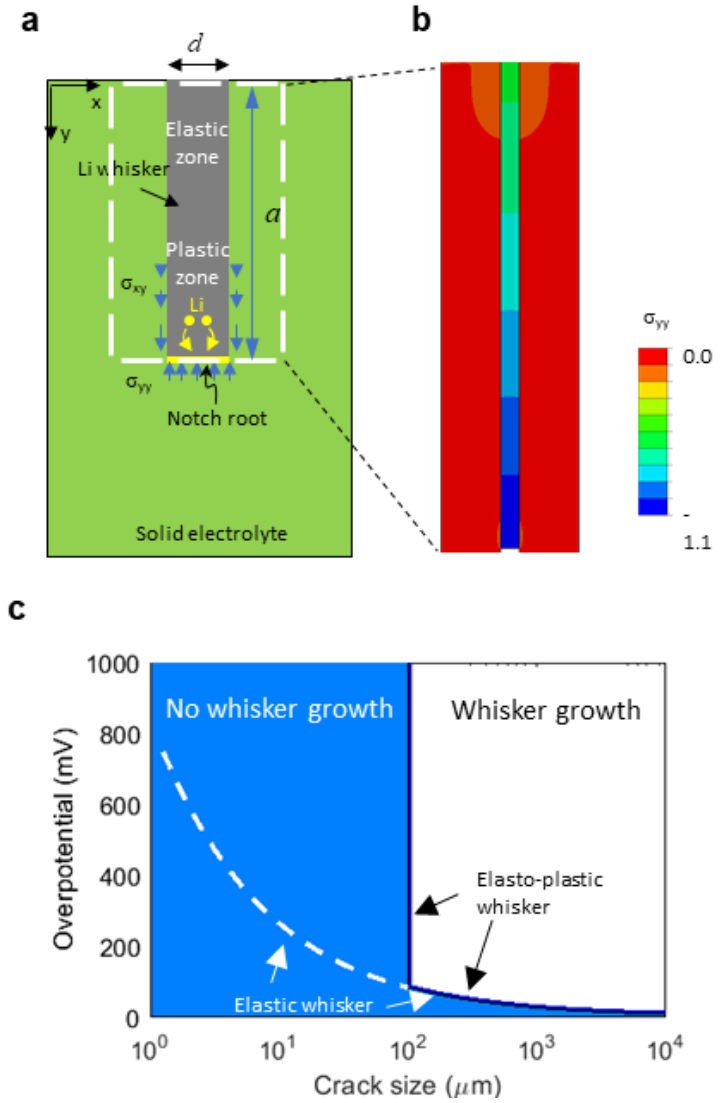

Figure 24 | Li whisker growth map based on an elasto-plastic whisker model in solid electrolyte. a, Schematic illustration of stress generation and fracture due to an elasto-plastic Li whisker (with length *a* and width *d*) growing into a main crack (with length *a*) in a solid electrolyte matrix. The high stress inside the Li whisker can cause its plastic yielding near the notch root of the main crack. The high stress in the solid electrolyte surrounding the growing tip of the Li whisker can trigger the extension of the main crack, leading to whisker growth. **b**, Finite element simulation result showing the contour of stress σ_{yy} (normalized by Young's modulus of Li) for the boxed region in (a), and the blue contour indicates the occurrence of plastic yielding in the tip of a central Li whisker embedded in a solid electrolyte of LLZO. **c**, A mechanism map of Li whisker growth in a solid electrolyte of LLZO in terms of overpotential and crack size, showing the domain without Li whisker growth (bounded by the blue solid line) predicted from of an elasto-plastic Li whisker model, compared with the prediction from an elastic Li whisker model (bounded by the white dashed line).

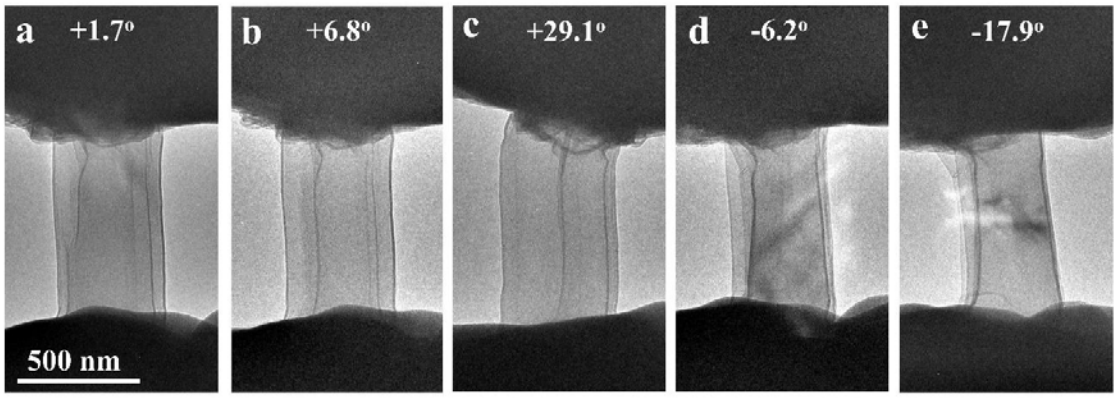

Figure 25 | Rotating an as-grown Li whisker to different angles to determining the cross-section shape of this whisker. By observing its projection images from different angles (**a**) +1.7°, (**b**) +6.8°, (**c**) +29.1°, (**d**) -6.2°, (**e**) -17.9°, we obtained the cross-section shape of the Li whisker.

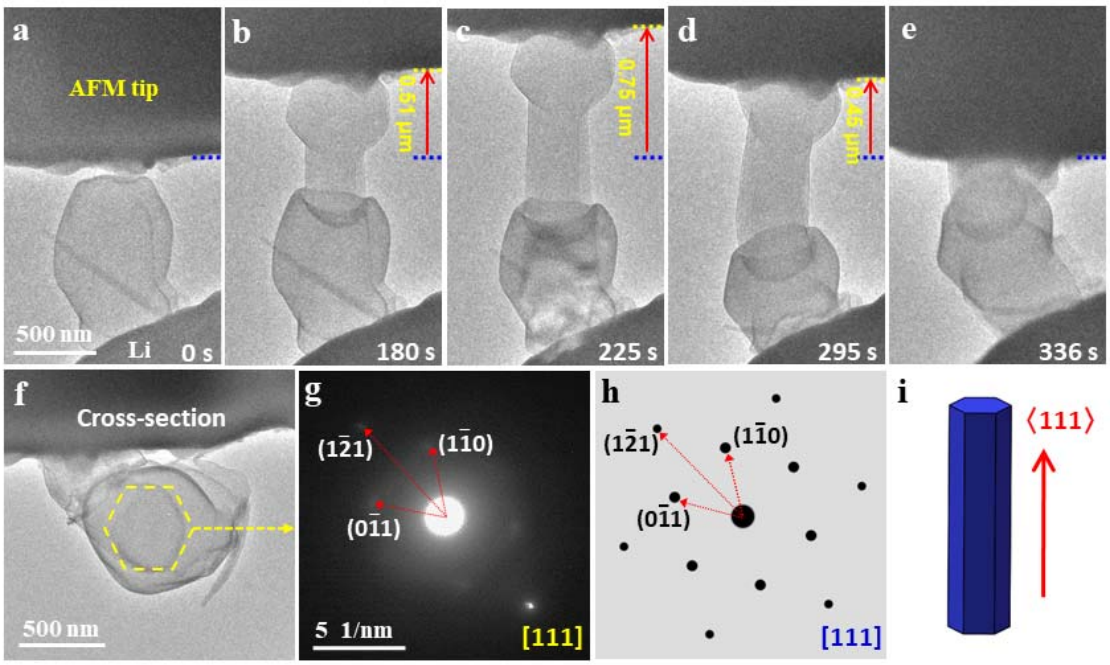

Figure 26 | *In situ* compression of the as-grown Li whisker. The whisker was manipulated to contact the AFM tip (**a**), causing growth of a secondary whisker over the old one at the bottom, pushing up against the AFM tip (**b-e**) under bias (k=3 N/m). Red arrowheads in (**b-e**) mark the displacement of the AFM tip. By pushing the lithium whisker to the AFM tip, the cross-section of the whisker turned into a perpendicular position to the electron beam. The cross-section shape of the whisker is hexagonal (**f**), and its growth direction is [111] (**g-i**).

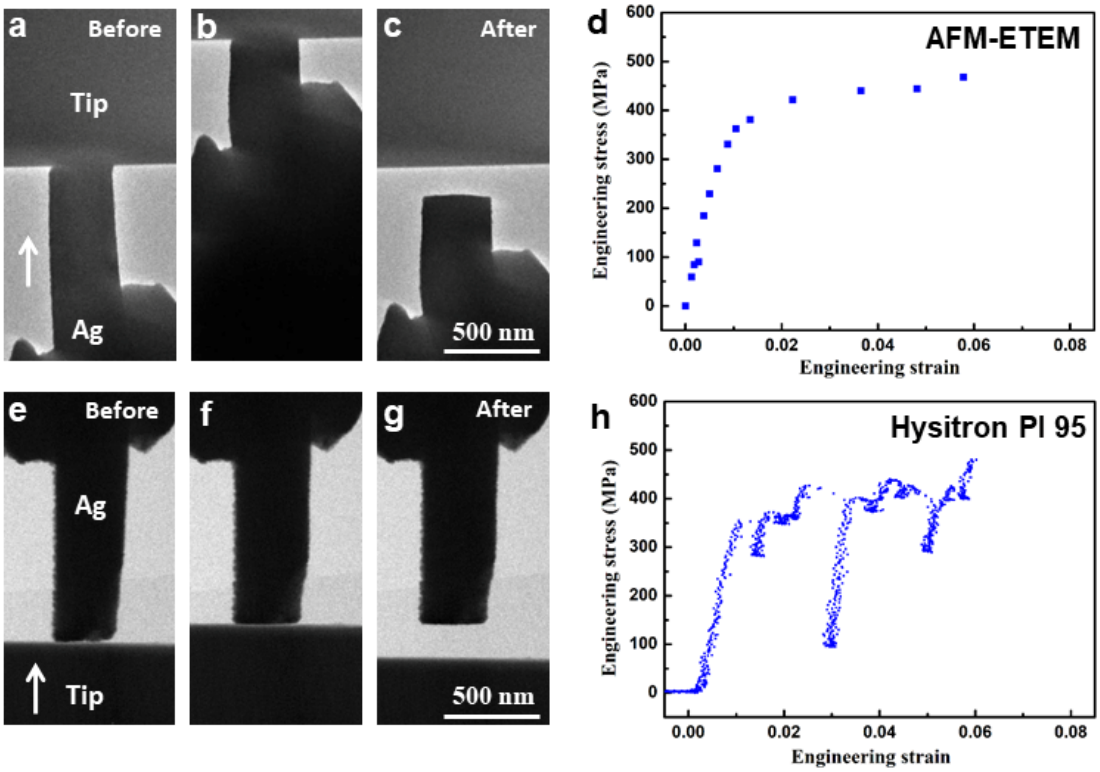

Figure 27 Benchmark experiments conducted on Ag pillars with the AFM-ETEM platform (a-d), and with a commercial mechanical testing TEM sample holder (Hysitron PI 95, e-h). (**a**, **e**), (**b**, **f**) and (**c**, **g**) are TEM micrographs of Ag pillars before, during and after compression, respectively. **d**, **h**, Stress-strain curves of Ag pillars obtained from compression experiments using the AFM-ETEM platform and a Hysitron PI 95 TEM holder, respectively. Note that strain burst was observed in the stress-strain curve obtained from the PI 95 holder, but not from the AFM-ETEM platform. This is because the detecting speed of the commercial Hysitron PI 95 is relatively fast and the number of collecting points are large, thus the generation of strain bursts (associated with dislocation avalanche[7] can be captured. However, for our AFM-ETEM device, due to the speed limit of data collection, the strain bursts have not been captured, but the measured yield stress and work hardening behavior are consistent with those from the Hysitron PI 95. It should be noted that nanoindentation produces non-uniform deformation beneath the indenter. Compression experiments conducted by the Hysitron PI 95 produces a more uniform deformation than nanoindentation, and the former provides a more quantitatively accurate measurement of mechanical properties. The Hysitron PI 95 is a well-established commercial mechanical property testing system for nanomaterials[8,9], so it can serve as a quantitative calibration for the AFM-ETEM testing platform.

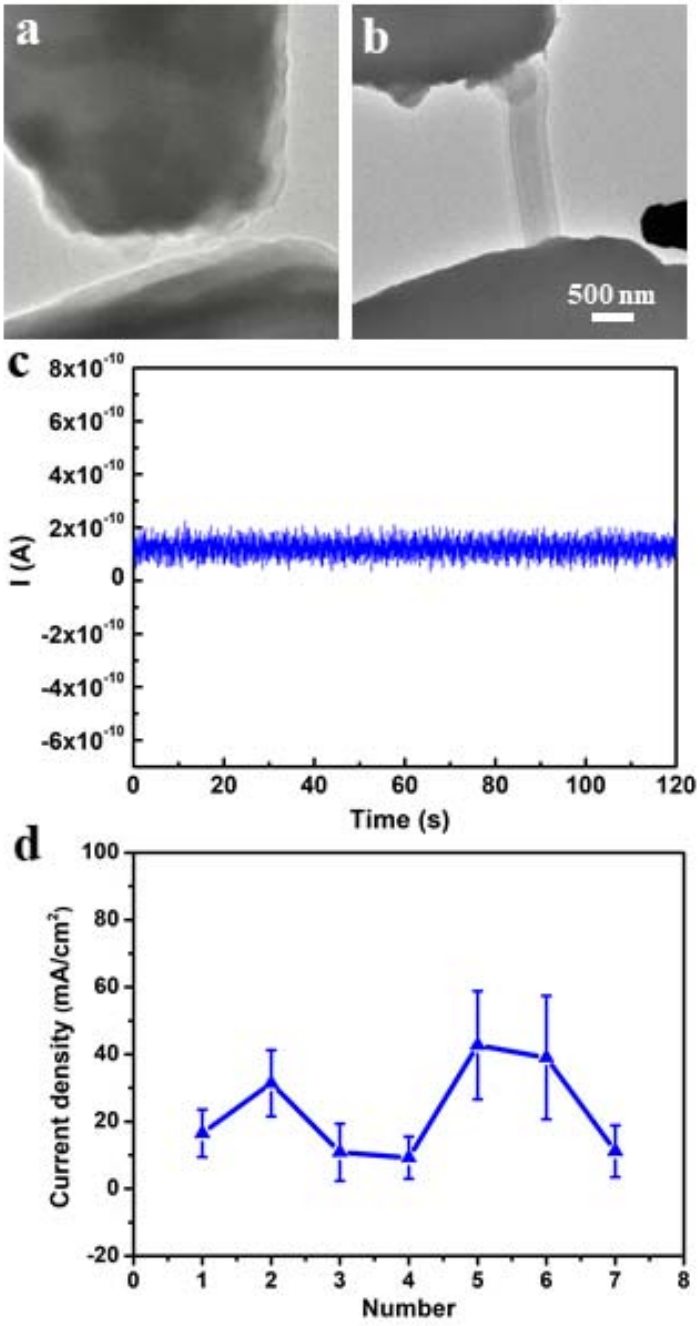

Figure 28 | a, **b**, *In situ* TEM images of Li whisker growth. **c**, The current flowing in the whisker. **d**, The average current density in seven whiskers.

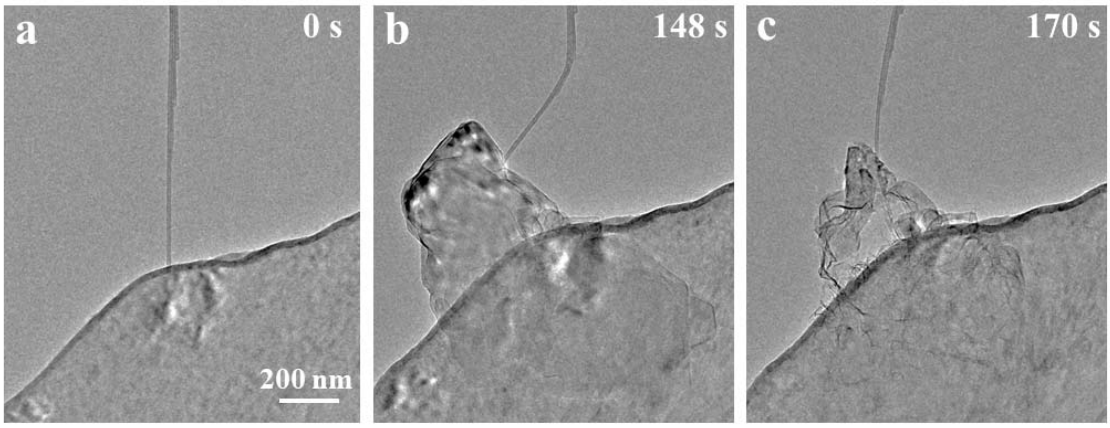

Figure 29 | a, Under a no-gas condition, a Li whisker does not grow, instead, only a Li plate grows. The Li plate was quickly broken under beam irradiation for 32 s. The experiment highlights the importance of the CO_2 gas and the formation of the surface Li_2CO_3 layer in facilitating the Li whisker growth and its subsequent stabilization.

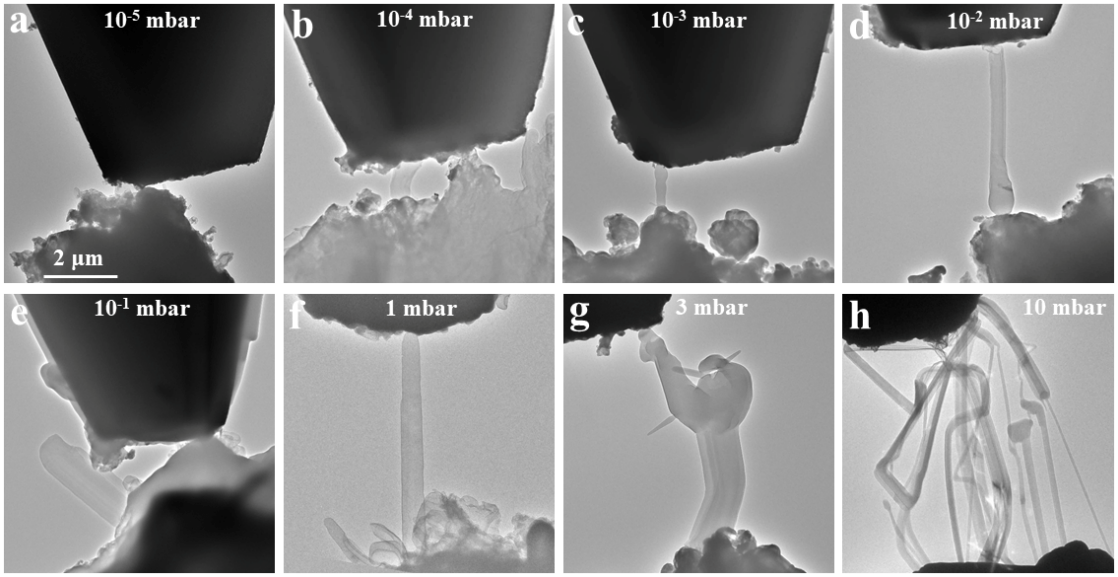

Figure 30 | *In situ* observations of growth of Li whiskers at different CO_2 pressures. TEM images showing no Li whisker growth at 10^{-5} mbar (**a**); individual Li whiskers grown at 10^{-4} mbar (**b**), 10^{-3} mbar (**c**), 10^{-2} mbar (**d**), 10^{-1} mbar (**e**), 1 mbar (**f**), 3 mbar (**g**), respectively; a number of weed-like Li whiskers grown concurrently at 10 mbar (**h**) of CO_2 pressure.

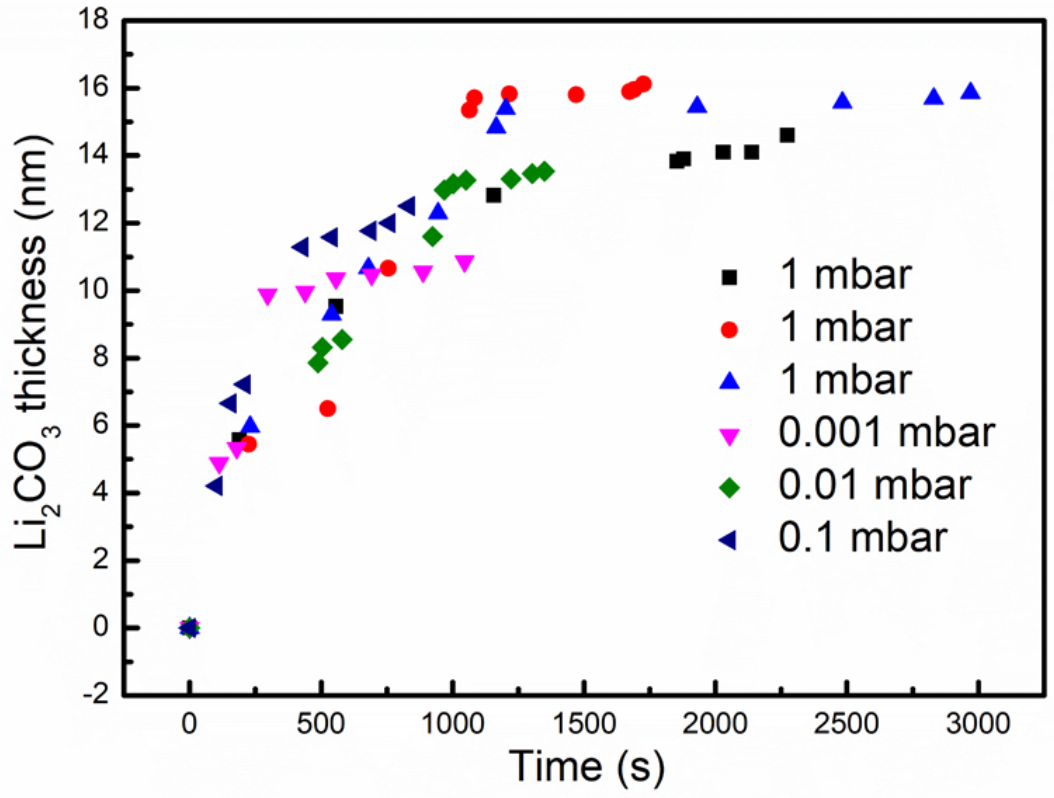

Figure 31 | Thickness of Li_2CO_3 passivation layer versus time at 1 mbar, 0.1 mbar, 0.01 mbar, 0.001 mbar, respectively.

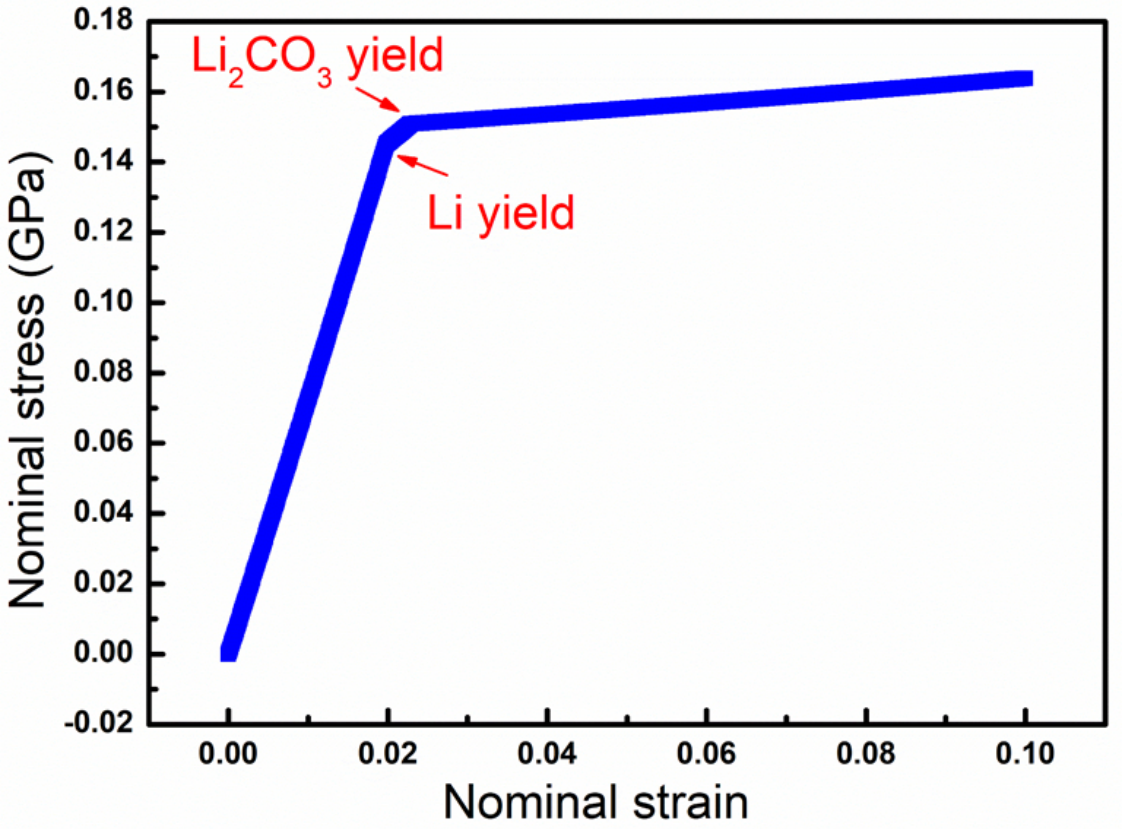

Figure 32 | Compressive stress-strain curve from a model of a Li/Li_2CO_3 whisker.

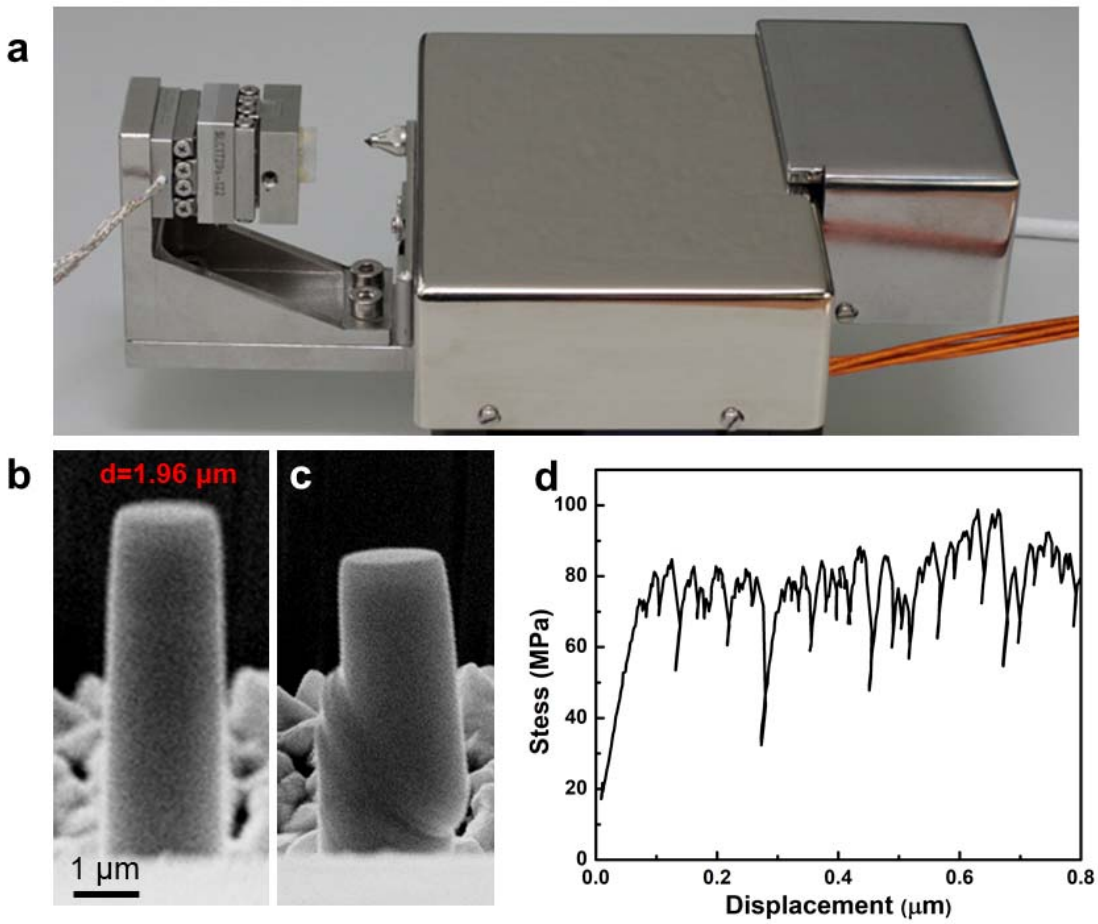

Figure 33 | Uniaxial compression experiment of a Li micro-pillar at room temperature. **a**, The compression experiment setup used in the SEM. **b** and **c** are representative SEM micrographs of a Li micro-pillar with a diameter of 1.96 μm before (left) and after (right) compression experiment, respectively. Note the large localized shear deformation occurred between the upper and lower part of the Li micro-pillar, which indicates that the yielding was caused by plastic deformation of the micro-pillar. **d**, Measured compressive stress versus displacement plot for the Li micro-pillar in (b-c).

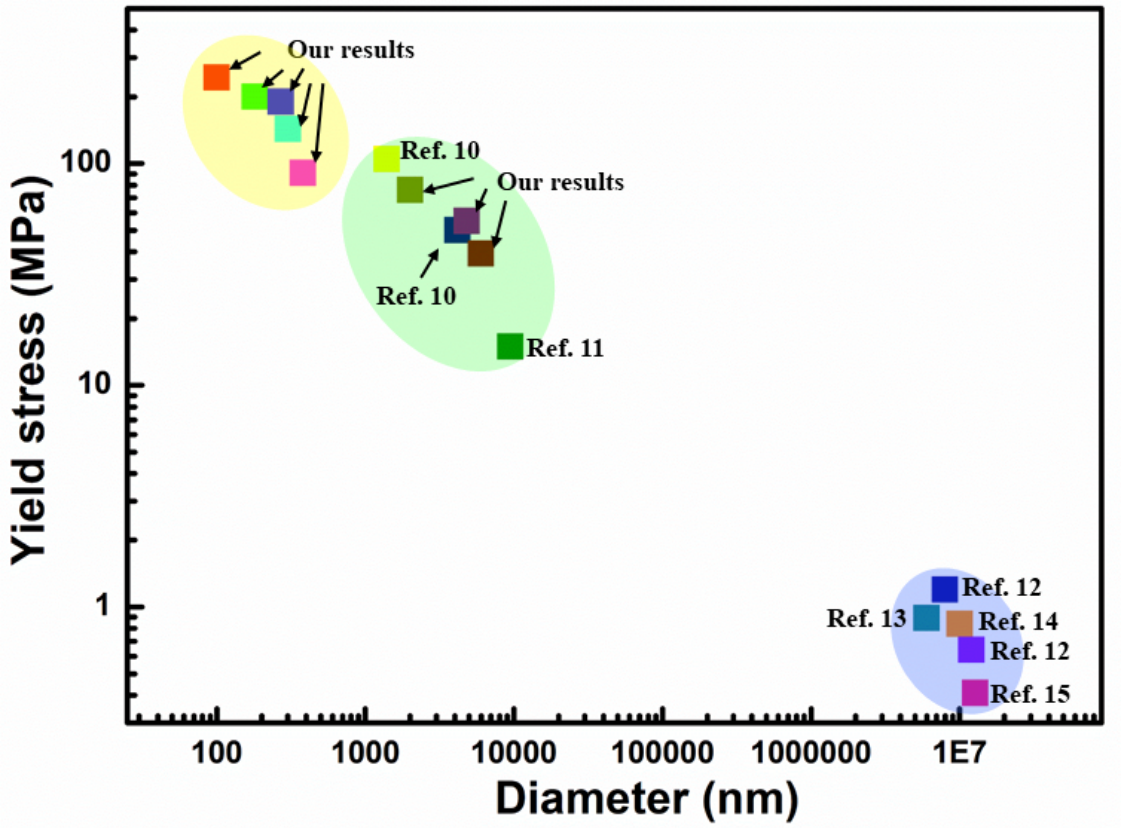

Figure 34 | Yield stress vs. diameter plot for Li metal across different length scales, showing an apparent size effect, i.e. smaller is stronger. The yellow circle encloses the data points from our testing of Li whiskers with diameter less than 1000 nm; the green circle encloses the data points of Li micro-pillars from the literature as well as our additional tests[10,11]; and the blue circle encloses the data points of bulk Li from the literatures[12-15].

References

1. Porz, L. *et al.* Mechanism of Lithium Metal Penetration through Inorganic Solid Electrolytes. *Adv. Energy Mater.* **7**, 1701003 (2017).
2. Cheng, E. J., Sharafi, A. & Sakamoto, J. Intergranular Li metal propagation through polycrystalline $Li_{6.25}Al_{0.25}La_3Zr_2O_{12}$ ceramic electrolyte. *Electrochim. Acta* **223**, 85-91 (2017).
3. Swamy, T. *et al.* Lithium Metal Penetration Induced by Electrodeposition through Solid Electrolytes: Example in Single-Crystal $Li_6La_3ZrTaO_{12}$ Garnet. *J. Electrochem. Soc.* **165**, A3648-A3655 (2018).
4. Han, F. *et al.* High electronic conductivity as the origin of lithium dendrite formation within solid electrolytes. *Nat. Energy* **4**, 187-196 (2019).
5. Tian, H.-K., Xu, B. & Qi, Y. Computational study of lithium nucleation tendency in $Li_7La_3Zr_2O_{12}$ (LLZO) and rational design of interlayer materials to prevent lithium dendrites. *J. Power Sources* **392**, 79-86 (2018).
6. Yang, T. T. *et al.* Air-Stable Lithium Spheres Produced by Electrochemical Plating. *Angew. Chem. Int. Ed.* **57**, 12750-12753 (2018).
7. Csikor, F. F., Motz, C., Weygand, D., Zaiser, M. & Zapperi, S. Dislocation avalanches, strain bursts, and the problem of plastic forming at the micrometer scale. *Science* **318**, 251-254 (2007).
8. Liu, B.-Y. *et al.* Large plasticity in magnesium mediated by pyramidal dislocations. *Science* **365**, 73-75 (2019).
9. Yu, Q. *et al.* Strong crystal size effect on deformation twinning. *Nature* **463**, 335-338 (2010).
10. Xu, C., Ahmad, Z., Aryanfar, A., Viswanathan, V. & Greer, J. R. Enhanced strength and temperature dependence of mechanical properties of Li at small scales and its implications for Li metal anodes. *Proc. Natl. Acad. Sci.* **114**, 57-61 (2017).
11. Xiang, B., Wang, L., Liu, G. & Minor, A. M. Electromechanical probing of Li/Li_2CO_3 core/shell particles in a TEM. *J. Electrochem. Soc.* **160**, A415-A419 (2013).
12. LePage, W. S. *et al.* Lithium Mechanics: Roles of Strain Rate and Temperature and Implications for Lithium Metal Batteries. *J. Electrochem. Soc.* **166**, A89-A97 (2019).
13. Tariq, S. *et al.* Li Material Testing- Fermilab Antiproton Source Lithium Collection Lens. *Particle Accelerator Conference* **3**, 1452-1454 (2003).
14. Masias, A., Felten, N., Garcia-Mendez, R., Wolfenstine, J. & Sakamoto, J. Elastic, plastic, and creep mechanical properties of lithium metal. *J. Mater. Sci.* **54**, 2585-2600 (2019).
15. Schultz, R. P. Lithium: Measurement of Young's Modulus and Yield Strength. *Report No. FERMILAB-TM-2191 (Fermi National Accelerator Lab.)* (2002).